

RESEARCH ARTICLE | SEPTEMBER 27 2018

Design considerations for indirectly driven double shell capsules

D. S. Montgomery; W. S. Daughton; B. J. Albright; ... et. al



Physics of Plasmas 25, 092706 (2018)

<https://doi.org/10.1063/1.5042478>

 CHORUS



View
Online



Export
Citation

CrossMark

Physics of Plasmas

Features in Plasma Physics Webinars

Register Today!

Design considerations for indirectly driven double shell capsules

D. S. Montgomery,¹ W. S. Daughton,¹ B. J. Albright,¹ A. N. Simakov,¹ D. C. Wilson,¹
 E. S. Dodd,¹ R. C. Kirkpatrick,¹ R. G. Watt,¹ M. A. Gunderson,¹ E. N. Loomis,¹
 E. C. Merritt,¹ T. Cardenas,¹ P. Amendt,² J. L. Milovich,² H. F. Robey,² R. E. Tipton,²
 and M. D. Rosen²

¹Los Alamos National Laboratory, Los Alamos, New Mexico 87545, USA

²Lawrence Livermore National Laboratory, Livermore, California 94551, USA

(Received 1 June 2018; accepted 7 September 2018; published online 27 September 2018)

Double shell capsules are predicted to ignite and burn at relatively low temperature (~ 3 keV) via volume ignition and are a potential low-convergence path to substantial α -heating and possibly ignition at the National Ignition Facility. Double shells consist of a dense, high-Z pusher, which first shock heats and then performs work due to changes in pressure and volume (PdV work) on deuterium-tritium gas, bringing the entire fuel volume to high pressure thermonuclear conditions near implosion stagnation. The high-Z pusher is accelerated via a shock and subsequent compression of an intervening foam cushion by an ablatively driven low-Z outer shell. A broad capsule design parameter space exists due to the inherent flexibility of potential materials for the outer and inner shells and foam cushion. This is narrowed down by design physics choices and the ability to fabricate and assemble the separate pieces forming a double shell capsule. We describe the key physics for good double shell performance, the trade-offs in various design choices, and the challenges for capsule fabrication. Both 1D and 2D calculations from radiation-hydrodynamic simulations are presented. *Published by AIP Publishing.* <https://doi.org/10.1063/1.5042478>

I. INTRODUCTION

The goal of inertial confinement fusion (ICF) experiments is to obtain a self-heating deuterium-tritium (D-T) plasma assembly in a laboratory setting and eventually demonstrate substantial burn of the D-T fuel and high energy gain for fusion energy applications. Most ICF concepts rely on the implosion of a spherical shell of some material that initially shocks and then heats the D-T fuel by compression to thermonuclear conditions, where the local heating by α -particles exceeds all other losses, the fusion reaction rate quickly rises, and a substantial fraction of the fuel burns before it can disassemble due to the extreme rising fuel pressure.

At the National Ignition Facility (NIF),^{1,2} up to 1.8 MJ of 351-nm laser light, in a 500-TW pulse, is available to indirectly drive single shell capsules. In indirect drive, the laser power is absorbed in a high-Z radiation case (hohlraum), generating x-rays which ablate and implode a spherical shell inward to high velocities (350–400 km/s). For single shell target designs,^{3–6} also called central hot spot ignition, an ablator shell (CH, Be or high-density carbon) of ~ 2 -mm diameter contains a cryogenic solid D-T fuel layer that is ~ 50 – 100 μ m thick. The solid D-T fuel layer ultimately acts as a spherical piston that first shocks then compresses and heats a central D-T gas, initially composed of D-T vapor. The solid D-T piston must be accelerated to >350 km/s while maintaining a low adiabat so that it can be compressed to high density and pressure when the dense fuel stagnates on the gas. Required hot spot convergence for single shell, central hot spot capsules is quite high, $CR \sim 40$, and any slight implosion drive asymmetries become magnified with these high convergences.

Unfortunately, maintaining drive symmetry throughout the high-convergence implosion has proven to be a challenge,⁷

such that kinetic energy of the implosion is not converted into sufficient internal fuel energy at stagnation, and fusion burn is not substantial. In addition, hydrodynamic instabilities and defects due to engineering features, such as the fill-tube and the thin membrane “tent” used to support the capsule, become exacerbated with convergence ratio, and further degrade conversion of kinetic energy to internal energy, or create a mix of high-Z materials into the D-T which quenches burn.⁷

As an intermediate goal to ignition and high fusion gain, demonstration of substantial self-heating (α -heating) of the D-T fuel is still challenging. Single shell implosions, with higher fuel adiabats than what is required for high gain capsules, have demonstrated the initial phases of α -heating⁸ but still require $CR > 30$ to substantially compress, form, and heat the D-T gas hot spot, and convert the implosion kinetic energy into hot spot internal energy. Double shell capsules, which employ a high-Z pusher to first shock and then compress and heat D-T gas, offer the potential for α -heating and robust burn of the D-T gas with a hot spot convergence $CR \sim 10$.^{9–11} As the name implies, the capsule consists of two nested shells with D-T fuel in the inner shell, as shown schematically in Fig. 1. While some of the challenges of high-convergence single shell capsules may be reduced or simplified by low-convergence double shells, the complications of fabricating the capsule and diagnosing a high-Z shell implosion increase substantially.

In this paper, we compare and contrast the physics of single shell, central hot spot ignition designs with double shell, volume ignition designs. We describe in general the idealized progression of a double shell implosion and develop simple physical models to estimate the performance at various stages. These simple models are compared to 1-D radiation hydrodynamic simulations and are shown to be

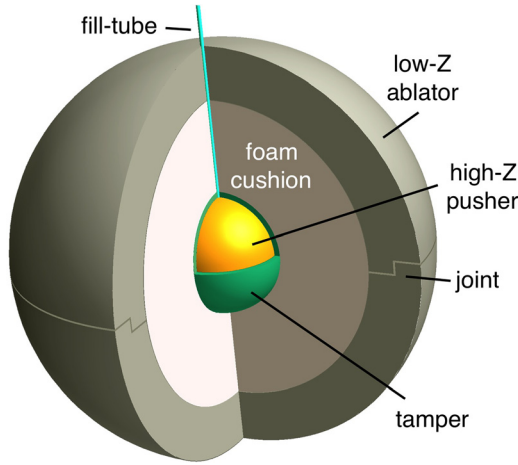


FIG. 1. Schematic of a double shell capsule. Inner shell is a high-Z material, with a low-Z tamper layer on the outside, or graded between the two materials for advanced designs. The inner shell is filled with D-T via a fill tube. A low-Z foam cushion surrounds the inner shell. The outer shell is an ablator and is made in two hemispheres, assembled around the inner shell and foam cushion.

sufficiently useful to make estimates of various implosion parameters. A metric for robust fusion burn is derived, which is compared to 2-D double shell simulations, and serves as a useful guide to identify designs that should perform either well or poorly in the presence of low-mode asymmetries.

II. POTENTIAL ADVANTAGES OF DOUBLE SHELLS

A. High-Z pushers

Consider for the sake of discussion that most ICF capsule designs, whether single shell ablators with a D-T fuel layer or double-shell capsules, can be idealized as the implosion of a 1-D spherical piston (pusher) of some material compressing D-T gas to thermonuclear conditions. As the pusher initially moves inward, it launches a shock into the D-T gas, setting an initial adiabat for the gas. Subsequent reflecting shocks within the gas can be approximated as quasi-isentropic compression of the D-T gas from an initial relatively high adiabat set by the first shock. As the pusher does work on the gas by changes in pressure and volume (PdV work) on the gas, the gas also does PdV work on the pusher, compressing it to high density. Near peak compression, the inward moving pusher stagnates as its pressure equilibrates with the pressure in the D-T gas.

As an illustrative estimate, suppose one wants the D-T gas to achieve 400 Gbar pressure (100 g/cm^3 at 5 keV). Since the pusher will reach this same pressure at stagnation, we want the pusher to remain as compressible as possible, i.e., nearly Fermi-degenerate. For this illustration purpose, the cold-curves from SESAME equation of state (EOS) tables are plotted in Fig. 2 considering pushers made from various solid materials: D-T ice, polystyrene, beryllium, aluminum, iron, and gold. At high compressed density, the pressure is determined mostly by Fermi-degeneracy of the electrons, scaling with electron density as $P \sim n_e^{5/3} \sim (\langle Z \rangle n_i / A)^{5/3}$, and will depend on the degree of ionization. If the pusher were compressed along the cold-curve, D-T would be compressed to about 1000 g/cm^3 at 400 Gbar, requiring a

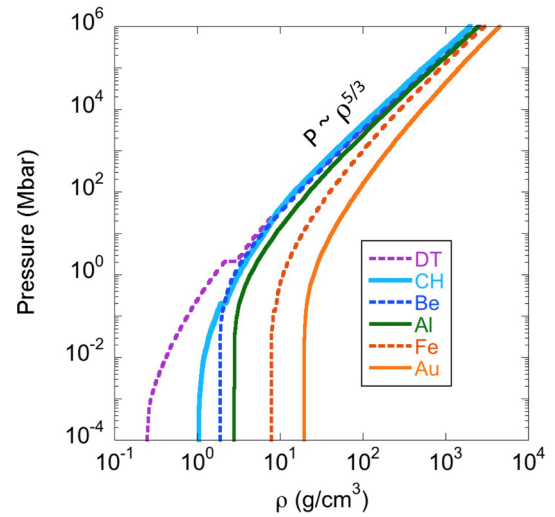


FIG. 2. Plot of cold compression curves of pressure versus material density from SESAME tables for D-T (dashed magenta), CH (solid light blue), Be (dashed dark blue), Al (solid green), Fe (dashed orange), and Au (solid gold). At the highest densities, the pressure roughly follows the expected trend for Fermi-degenerate electrons.

compression of 4000 starting from an initial solid density of 0.25 g/cm^3 . At the extreme, Au would be compressed to about 2000 g/cm^3 at 400 Gbar, requiring a compression of ~ 100 from an initial density of 19.3 g/cm^3 . Thus, a dense, high-Z pusher requires less compression, and less convergence, to achieve a similar D-T hot spot pressure at stagnation as a low density, low-Z pusher.¹² Assuming a thin shell pusher, where the compression varies as the square of the gas convergence ratio, CR^2 , a high-Z pusher such as Au will have a D-T gas (hot spot) convergence ratio $CR \sim 10$, whereas a D-T pusher would require a hot spot convergence $CR \sim 60$. These crude estimates are comparable to those found in radiation-hydrodynamic design simulations. Double shell capsule designs show a hot spot $CR \sim 10$ in our designs (α -heating off), while for low-adiabat Be and CH single shell capsules that are calculated to ignite,^{13,14} the hot spot $CR \sim 40$.

The pusher equation of state can inform other required implosion parameters, such as the minimum required implosion velocity.¹² Figure 3 shows the cold curves of specific internal energy versus pressure for D-T and Au. For an optimized implosion, the pusher adiabat should closely follow the cold curve at high pressures, so these cold curves will be sufficient for simple illustrative purposes. Assume a desired hot spot pressure of 400 Gbar at stagnation (in the absence of alpha deposition), and an isobaric configuration for the pusher and hot spot. At stagnation, the kinetic energy of the pusher becomes internal energy in the pusher and gas, $KE_p \approx IE_p + IE_{gas}$. If roughly half of the kinetic energy ends up as internal energy of the pusher, $IE_p \sim 1/2 KE_p$, then $v_{imp} \approx 2\sqrt{IE_p/M_p}$, where M_p is the pusher mass. At 400 Gbar, the specific internal energy for Au is 12 000 MJ/kg, giving $v_{imp} \sim 220 \text{ km/s}$. For a D-T pusher at 400 Gbar, the specific internal energy is 34 500 MJ/kg, yielding $v_{imp} \sim 370 \text{ km/s}$. These implosion speeds are in rough agreement with those found in optimized radiation-hydrodynamic simulations.

In addition, a D-T hot spot surrounded by a dense, high-Z pusher experiences less radiative and conductive losses

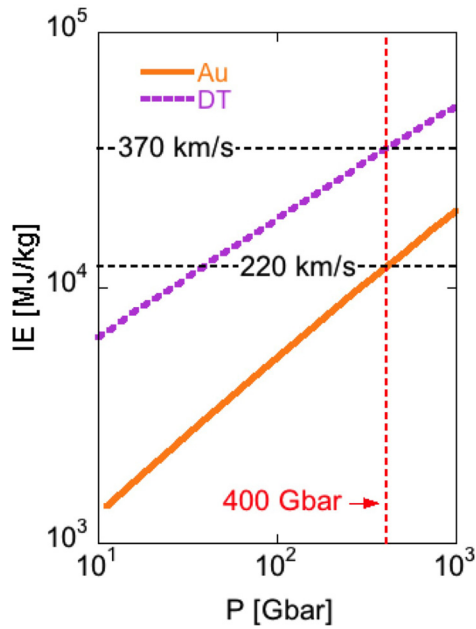


FIG. 3. Plot of cold compression curves of specific internal energy versus pressure from SESAME tables for D-T (dashed magenta) and Au (solid gold). The vertical red dashed line represents 400 Gbar pressure, and the horizontal dashed lines are the specific internal energies at 400 Gbar, labeled as pusher velocities, assuming $1/2$ of the pusher kinetic energy turns into internal energy in the pusher at stagnation.

than a low- Z pusher for the same hot spot volume and area. The power loss per unit volume (power density) from thermal conduction is estimated by Lindl³ as $P_C = QA/V = 3Q/r$, where $Q = -\kappa \nabla T = -(C_1 S(Z)/Z \cdot \ln \Lambda) T^{5/2} \nabla T$ is the Spitzer-Härm electron thermal heat flux, $C_1 = 9.4 \times 10^{12}$, and Q in units of W/cm^2 . The electron-ion transport correction term $S(Z)$ varies from 1.0 at $Z=1$ to 4.0 for $Z \gg 1$; thus, the thermal conduction loss is an order of magnitude less for a hot D-T plasma conducting into a dense, cooler high- Z pusher ($Z \sim 40$) than for a $Z=1$ pusher (dense, D-T fuel) of the same area and volume. For radiative losses, a high- Z pusher is orders of magnitude more opaque to radiation than a $Z=1$ pusher. A Marshak wave penetrates the high- Z pusher and reradiates most of the absorbed flux, i.e., the radiation is trapped within the hot spot volume, as opposed to a low- Z transparent pusher where the radiation is effectively lost.

B. Progression of an idealized double shell implosion

Figure 4(a) shows a radius versus time (r - t) diagram of Lagrangian zones for a typical 1-D double shell capsule. A contour plot (shock plot) of the logarithmic derivative of material density, $(1/\rho)(\partial\rho/\partial r)$, versus Lagrangian index and time is shown in Fig. 4(b). The double shell capsule implosion progresses as follows:

- (i) radiation incident on the outer shell (ablator) is absorbed and ablates shell material, and drives an ablative shock inward;
- (ii) the ablation-driven shock breaks out from the outer shell, launching a shock wave inward into the foam cushion, and the outer shell begins to accelerate inward;

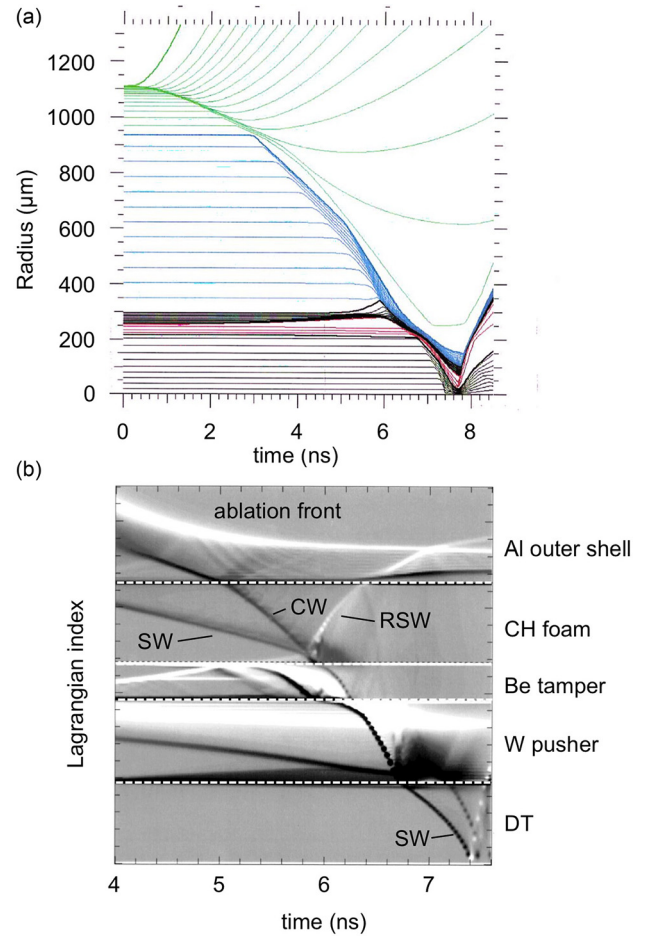


FIG. 4. A radius versus time plot for the fall-line optimized double shell design shown in (a). Contours of the logarithmic derivative of material density versus Lagrangian index and time for the fall-line optimized design shown in (b), so-called shock plots. Some of the main shock waves (SW), compression waves (CW), and reflected shock waves (RSW) are labeled.

- (iii) an outward going rarefaction wave is also launched from the ablator-foam interface. It encounters the high-pressure ablation front and reflects a compression wave travelling inward, further accelerating the outer shell;
- (iv) the initial shock in the foam is overtaken by the compression wave driven shock. This main shock impinges on the dense, inner shell (pusher), transmitting a forward going shock towards the D-T gas, and reflecting a shock traveling out towards the outer shell;
- (v) the foam is compressed quasi-adiabatically by the outer shell, generating a large, pressure reservoir exterior to the inner shell;
- (vi) when the shock breaks out from the inner shell into the fuel, it begins to accelerate inward from the pressure in the foam, gaining kinetic energy, and initially compressing the D-T gas;
- (vii) the inner shell reaches maximum kinetic energy when the D-T gas pressure exceeds the drive pressure in the foam. This roughly coincides with the arrival of the reflected outgoing shock at the inner shell/gas interface. The inner shell begins to decelerate;

- (viii) the inner shell does PdV work on the gas, compressing and heating it, as the gas does PdV work on the shell, compressing it;
- (ix) implosion stagnation occurs when the gas pressure and inner shell pressure are equal. The fuel reaches its maximum internal energy due to shock and compression heating (in the absence of alpha heating).
- (x) fusion burn starts during the deceleration phase (vii), and is completed during stagnation phase.

This encapsulates the idealized, 1D implosion of a double shell. At minimum, one wants sufficient fuel areal density, $\rho R > 0.3 \text{ g/cm}^2$, and ion temperature ($T_i > 2.5 \text{ keV}$) so that alpha deposition from D-T fusion in the hot spot exceeds radiation and conduction losses. The conditions for robust fusion burn, insensitive to low mode asymmetries during the stagnation phase, will be discussed later in the paper.

C. Comparison to single shell, central hot spot designs

While there are many similarities between a single shell and a double shell implosion, both conceptually idealized as a 1D spherical piston compressing and heating D-T gas, several key differences are worth noting. There are both potential advantages and disadvantages for the physical mechanisms involved, and the ability to fabricate the capsules and diagnose the implosions experimentally.

One possible advantage of a double shell capsule, already discussed, is the lower hot spot convergence ratio. Lower convergence implies less sensitivity to low-mode asymmetry, as well as less potential mix at the pusher/gas interface during deceleration phase. Double shell capsule designs optimized for “fall-line” are calculated to have fusion burn occurring early during the deceleration phase prior to stagnation, before low mode asymmetries can further grow, and before possible mix at the pusher/gas interface can penetrate the hot spot. A metric for robust burn will be described later in the paper.

It is worth noting that the traditional concept of total convergence ratio for a double shell, defined as the outer ablator radius to hot spot radius, can be larger than that for a single shell, $CR_{\text{Tot}} \sim 55$ for our fall-line optimized double shell versus $CR_{\text{Tot}} \sim 40$ for a typical single shell. However, we find that a naïve application of CR_{Tot} as a figure of merit for symmetry requirements for a double shell is overly restrictive since material is not being moved over this entire convergence. After the ablatively driven shock passes through the foam cushion, its sound speed $\sim 200 \text{ km/s}$ is comparable to the outer shell implosion speed. This allows pressure perturbations during foam compression, driven by outer shell asymmetry, to smooth out to some degree before acceleration of the inner shell. Indeed, 2D integrated calculations indicate that outer shell asymmetry $P_2/P_0, P_4/P_0 \sim 5\%$ at the time of collision with the inner shell still leads to acceptable hot spot asymmetries $< 30\%$. Further details of the 2D symmetry requirements are beyond the scope of this present paper, whose main focus is on the 1D physics of double shells.

The pusher acceleration mechanism for a double shell capsule differs greatly from a single shell and may offer several potential advantages by reducing uncertainties in the

physics. In a single shell capsule, one can consider the cryogenic D-T ice layer ($\rho_0 = 0.25 \text{ g/cm}^3$) as the “pusher,” initially shocking and compressing the D-T gas. There are several physics challenges and possible uncertainties in accelerating the D-T ice pusher to the required 350–400 km/s velocities to ignite the D-T gas, beyond the large hot spot convergence already discussed. The D-T pusher in a single shell target is ablatively driven, with the D-T pusher being in intimate contact with the ablator material. From a design perspective, one needs to accurately calculate the radiation field driving the ablator and understand the radiation drive as a function of angle, spectrum, and time at the ablator surface. Uncertainties in the ablator opacity, radiation transport, or non-Planckian aspects of the radiation field (hohlraum M-band) are exacerbated by the required high convergence of an ablatively driven low-Z pusher. Since the D-T pusher is driven by a relatively hot, ablated plasma, uncertainties in thermal conduction from the ablation region to the cold, dense pusher can place uncertainties on the conditions of the pusher during acceleration and deceleration phases.^{7,15} In addition, a D-T pusher is very susceptible to hot electron preheat due to laser-plasma instabilities during the acceleration phase,¹⁶ and must be kept on a sufficiently low adiabat to reach high pressure at stagnation and high areal density for confinement.⁶ Finally, a D-T pusher must be accelerated by several shocks in precise succession, launched by an accurately shaped radiation pulse, so that the pusher remains on a nearly Fermi-degenerate adiabat during acceleration phase.^{6,16}

In contrast, the high-Z pusher (inner shell) of a double shell is hydrodynamically driven, initially by the main shock from ablation at the outer shell, then further driven by the increasing pressure in the foam cushion as the outer shell compresses it after converging only a factor of a few. The conditions of the ablatively driven outer shell are much less susceptible to the aforementioned uncertainties for single shells due to its very low convergence ($CR \sim 3\text{--}4$). The ablation process is decoupled from the high-Z pusher, reducing uncertainties in the condition of the pusher due to radiation and thermal transport. The high-Z pusher is impervious to hot electron preheat from laser plasma instabilities (LPI). While preheat of the high-Z pusher does matter, either by hard x-rays or LPI hot electrons penetrating the outer shell, the preheat is absorbed in the outer few microns of the high-Z inner shell. However, the preheat does not directly affect the adiabat of the high-Z pusher. Compared to a D-T pusher ($Z = 1$), a high-Z pusher such as tungsten ($Z = 74$) or gold ($Z = 79$) is Fermi-degenerate during the deceleration and stagnation phase due to its large number of electrons and large heat capacity. A Thomas-Fermi like EOS model for Au (see Appendix A), as an example, shows the ionization state due to pressure ionization is $Z^* \approx 5.1\rho_{\text{Au}}^{0.274}$. For Au compressed to 2000 g/cm^3 at stagnation, the ionization state is $Z^* \sim 40$, the Fermi temperature due to electron degeneracy is approximately $\epsilon_F \approx 7.9(n_e/10^{23})^{2/3} \text{ eV}$, and we find for an electron density $n_e = 2.5 \times 10^{26} \text{ e/cm}^3$ a Fermi temperature $\epsilon_F \approx 1.5 \text{ keV}$. For most double shell designs, the dense high-Z pusher at stagnation has an average thermal temperature of 0.5–0.7 keV so that the shell is completely Fermi

degenerate, despite multi-Gbar drive pressures during the acceleration phase.

Unlike a D-T pusher, a high-Z pusher of a double shell is accelerated to ~ 250 km/s with an initial strong shock and increasing pressure in the foam cushion, effectively an impulsive drive that is internally pulse-shaped by the cushion, as opposed to the carefully tailored external 4-shock drive pulses required to accelerate a D-T pusher while keeping it at best $1.5\times$ Fermi degenerate. As a result, the laser pulse for a double shell capsule is only a few ns duration, and therefore, less susceptible to loss of drive and radiation symmetry due to LPI losses. A double shell can be filled with D-T gas or cryogenic D-T liquid, thus not requiring a cryogenic solid D-T layer, so that uncertainties in the mass added to the hot spot during the stagnation phase are removed.¹⁷ A double shell capsule is calculated to ignite via volume ignition with the electron, ion, and radiation temperatures in equilibrium at ignition ($T_e \sim T_i \sim T_r$). A single shell capsule with a D-T pusher ignites out of equilibrium ($T_i > T_e > T_r$) and requires the D-T hot spot to form mostly out of the dense D-T pusher at stagnation, with burn propagation from the central hot spot towards the dense D-T fuel.

The trade-offs in physics uncertainties for double shells compared to single shells with a D-T pusher make them an attractive alternative for obtaining robust burn with runaway alpha-heating and possibly ignition, albeit at a reduced gain ($G \sim 1$) compared to single shell capsules with a D-T fuel layer. However, those potential physics advantages are traded for increased risks in target fabrication, in diagnosing the dense, high-Z shell as it implodes, as well as the potential risk for high-Z mix into the D-T fuel. Table I summarizes the trade-offs for double shell versus single shell capsules below.

Compared to single shell targets, double shells have multiple interfaces, with reflecting shock and rarefaction waves between these surfaces, which appear to make double shells daunting to understand. In Secs. III–VI, we develop and describe simple physical models to make useful estimates for various stages of a double shell implosion and its performance, which helps guide understanding for trade-offs between various design parameters.

TABLE I. Performance trade-offs between double shell (volume ignition) capsules and single shell (central hot spot ignition) capsules.

Performance/design metrics	Double shell	Single shell
Hot spot convergence ratio	CR ~ 10	CR > 35
Pusher implosion speed	~ 250 km/s	> 380 km/s
Pulse shape, shock timing	impulsive, few ns	3–4 shock, 7–20 ns
Sensitivity to LPI/asymmetry	Low	High
Sensitivity to uncertainties in ablative-drive physics	Low	High
Requires fuel layer?	No	Yes
Sensitivity to mix at gas-pusher interface	Most sensitive	Least sensitive
Capsule fabrication	Most challenging	Least challenging
Diagnosing implosion	Most challenging	Less challenging

III. ABLATION AND PREHEAT RISKS

For a fixed drive energy, such as the NIF laser, and using indirect drive, double shell performance benefits from maximizing the absorbed energy in the ablator, and maximizing the kinetic energy of the remaining ablator mass. While low-Z ablators such as CH and Be appear to be ideal for this, the hard x-ray preheat from hohlraum M-band and L-band, at 2.5 keV and 10 keV for a Au hohlraum, readily penetrates these low-Z outer shells and are absorbed by the exterior of the high-Z inner shell. The preheated high-Z material will expand outward in the foam and will be recompressed by both the main shock and the compression of the outer shell as it collides with the inner shell. From a 1D physics perspective, preheat expansion of the inner shell wastes energy by recompressing the expanded material during shock and outer shell collision. From a 2D/3D perspective, non-uniform preheat of the inner shell imposes asymmetries on the inner shell during the acceleration and deceleration phases that cannot be tuned by radiation drive symmetry on the outer shell. Preheat expansion of the high-Z shell also increases the risk of Richtmyer-Meshkov instability as the main shock encounters this expanded material, giving the instability more time to grow.¹¹

Adding mid-Z or high-Z dopants to the outer ablator can mitigate x-ray preheat,⁹ mostly from M-band. While single shell capsules, made by sputtering or vapor deposition techniques, can easily manufacture dopant layers within the ablator and leave its outer regions pure low-Z material, such fabrication techniques are not amenable for making machinable hemispheres for the outer shell, as discussed later in Sec. VII. Thus, uniformly doped outer ablators, that are machinable, are required for the outer shell.

The need for high ablation efficiency (low albedo) and high opacity to hard x-rays presents conflicting requirements for the choice of ablator materials. Materials considered for the outer ablator have been copper-doped beryllium (Be:Cu), aluminum-doped beryllium (Be:Al), and various alloys of aluminum, ranging from pure Al to Al alloyed with mid-Z elements to improve strength. Since x-ray re-emission goes as $\langle Z \rangle^2$, higher average $\langle Z \rangle$ ablators have better hard x-ray preheat shielding but perform worse for ablation efficiency due to their higher average albedo. The trade-offs in physics considerations and target fabrication considerations for ablator materials will be discussed further in Sec. VII.

For a given ablator choice, the outer shell radius and hohlraum drive temperature determine its resultant kinetic energy of the ingoing shell,¹⁸ with $E_{\text{abs}} \sim R_{\text{out}}^2 T_r^{2.5}$. For these present designs, we considered $R_{\text{out}} = 1.11$ -mm outer shells driven in a 5.75-mm diameter cylindrical Au hohlraum with peak radiation temperature $T_r \sim 300$ eV. The capsule diameter was chosen based on previous experiments that demonstrated good implosion symmetry for this size of capsule. A 5-ns reverse ramp pulse shape was used, with peak power ~ 450 TW, to provide a roughly constant radiation temperature with time. The laser pulse reaches peak power early in time for a reverse ramp pulse shape, minimizing the risk for LPI since the hohlraum wall plasma has had little time to expand.

A series of 1D capsule only simulations were performed using the radiation-hydrodynamics code HYDRA¹⁹ and a frequency-dependent source derived (FDS) from 2D integrated hohlraum calculations. The FDS source and outer shell radius of 1.11-mm were fixed. CH foam with 0.035 g/cm³ density was chosen for the cushion based on current fabrication constraints. A tungsten inner shell was chosen ($Z = 74$, $\rho = 19.3$ g/cm³) based on fabrication constraints, and a beryllium layer was added to the exterior of the inner shell to tamp any possible preheat expansion,⁹ and mitigate Richtmyer-Meshkov (RM)-instability by having a lower Atwood number at the foam/inner shell interface.¹¹ The D-T fill was varied between 0.173 and 0.24 g/cm³, within the current NIF cryogenic target fill capability. Hundreds of simulations were performed to optimize either for fusion yield, or for best fall-line performance.^{10,11} The simulations varied the outer shell thickness, the radius and thickness of the inner shell, the tamper thickness, and the fuel density. The optimum designs had an ablator remaining mass of 13%–15%. Assuming a simple rocket model with a constant ablation rate, the outer shell implosion velocity is $U = U_{ex} \ln(M_0/M)$, where M_0 is the initial ablator mass, M is the remaining mass (payload mass), and U_{ex} is the exhaust velocity of the ablated material. The kinetic energy of the remaining mass is then $1/2 M [U_{ex} \ln(M_0/M)]^2$, which maximizes when $M/M_0 = 1/e^2 \approx 0.135$.

IV. KINETIC ENERGY TRANSFER

A. Main shock

After the main ablatively driven shock breaks out of the outer shell, it launches an inward propagating shock into the foam. An outward going rarefaction wave propagates from the outer shell/foam interface and after encountering the ablation front, it is reflected as an inward going compression wave. At the outer-shell/foam interface, it launches a 2nd, stronger shock inward, and further accelerates the outer shell. The stronger shock overtakes the initial shock in the foam and forms what we term as the main shock.

When the main shock reaches the dense, high- Z inner shell, a shock is transmitted inward into the inner shell, and reflected outward through the foam. Since the main shock collision with the inner shell sets the initial adiabat of the inner shell and begins its acceleration phase, we make estimates of its characteristics.

As an idealization of the problem, consider a strong shock in a low density gas, region A with density ρ_A , propagating inwards and incident on a high density barrier, region B with density ρ_B , such that $\rho_A < \rho_B$. We consider planar propagation only and ignore convergence effects.

Behind the shock in the low-density region, the particle speed is u_1 , shock speed is $u_s = u_1(\gamma + 1)/2$, the pressure is P_1 , and the shocked density is $\rho_1 = \rho_A(\gamma + 1)/(\gamma - 1)$. This can be treated as a block of plasma at density and pressure (ρ_1, P_1) moving inwards at speed u_1 . The *principal* Hugoniot for the low density and high density regions, in the strong shock limit, are

$$P_A = \left(\frac{\gamma + 1}{2} \right) \rho_A u^2, \quad (1a)$$

$$P_B = \left(\frac{\gamma + 1}{2} \right) \rho_B u^2. \quad (1b)$$

The reflected shock Hugoniot must pass through the points (u_1, P_1) and $(0, P_{Rmax})$, where the latter is the classic result of von Neumann²⁰ of completely stagnated shock flow from a rigid wall, $\rho_B \rightarrow \infty$. In the case of a rigid wall, the reflected shock pressure, for stagnated flow $u = 0$, is

$$\frac{P_{Rmax}}{P_1} = \left(\frac{3\gamma - 1}{\gamma - 1} \right). \quad (2)$$

We find the *reflected* Hugoniot in the shocked, low density material (region A) to be

$$P_R = \left[\left(\frac{3\gamma - 1}{\gamma - 1} \right) P_1 - \left(\frac{\gamma + 1}{\gamma - 1} \right) \rho_A u_s^2 \right] + \left(\frac{\gamma + 1}{\gamma - 1} \right) \rho_A (u_s - u)^2, \quad (3)$$

where the first term in square brackets is a constant initial pressure for the reflected Hugoniot (dependent on initial parameters), and the second term is the particle speed-dependent portion of the *reflected* Hugoniot, starting at an initial shocked density of $\rho_A(\gamma + 1/\gamma - 1)$.

Rewriting to parameterize the initial pressure in terms of only ρ_A , u_1 , we arrive at the *reflected* Hugoniot for the low density region A

$$P_R = \left(\frac{\gamma + 1}{\gamma - 1} \right) \rho_A (u_s - u)^2 + \frac{(\gamma + 1)(3 - \gamma)}{4} \rho_A u_1^2. \quad (4)$$

As the shock encounters the dense barrier of region B, continuity of both pressure and particle speed *must exist* at the contact discontinuity. To find the reflected pressure and particle speed from the shock hitting the region B barrier, we equate the *reflected* Hugoniot of region A (reflected shock) to the *principal* Hugoniot of region B (transmitted shock), i.e., $P_R = P_B$. Plotted on Fig. 5(a) are the *principal* Hugoniot for regions A and B, and the *reflected* Hugoniot for region A, illustrating this for $P_1 = 20$ Mbar, $u_1 = 173$ km/s for $\rho_A = 0.05$ g/cm³ and $\rho_B = 10$ g/cm³, $\gamma = (5/3)$.

The equated reflected and transmitted pressures, using the *reflected* Hugoniot for region A and the *principal* Hugoniot for region B, are written as

$$P_R = \left(\frac{\gamma + 1}{\gamma - 1} \right) \rho_A (u_s - u)^2 + \frac{(\gamma + 1)(3 - \gamma)}{4} \rho_A u_1^2 = \left(\frac{\gamma + 1}{2} \right) \rho_B u^2. \quad (5)$$

Since the transmitted and reflected pressures and particle speeds are equal

$$\frac{P_R}{P_1} = \frac{P_T}{P_1} = \frac{\rho_B u^2}{\rho_A u_1^2},$$

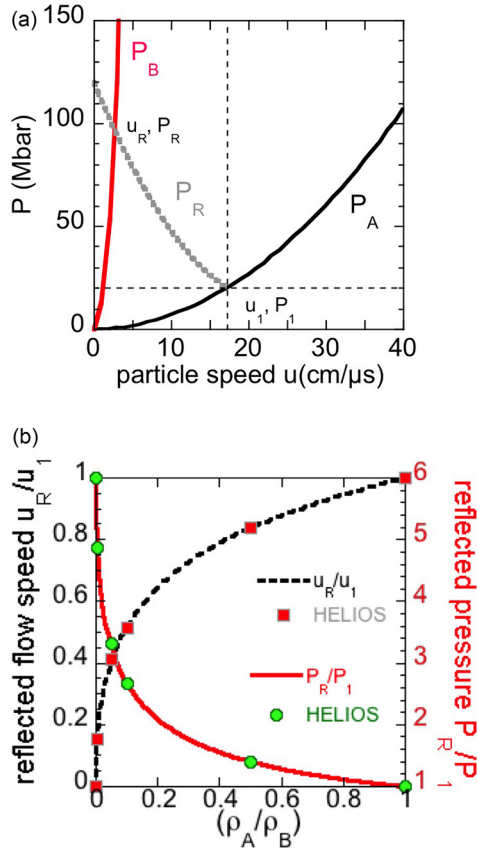


FIG. 5. (a) Theoretical Hugoniot plots for materials A and B with $\rho_B > \rho_A$ shown in black and red, and the reflected shock Hugoniot (dashed gray) for a shock propagating in material A and reflecting off material B. (b) Theoretical impeded flow and reflected/transmitted shock pressure versus density ratio. The data points are from 1-D HELIOS simulations, and the curves are theory from Eq. (7).

we parameterize the solution in terms of the impeded transmitted flow with respect to the incident flow, (u/u_1) and the ratio of the initial densities (ρ_A/ρ_B)

$$\left(\frac{u}{u_1}\right)^2 = \left(\frac{\rho_A}{\rho_B}\right) \left[\frac{(3-\gamma)}{2} + \frac{(u_s - u)^2}{u_1^2} \left(\frac{2}{\gamma-1} \right) \right]. \quad (6)$$

Solving solely for the impeded flow (u/u_1)

$$\frac{u}{u_1} = \frac{\sqrt{\frac{\rho_A}{\rho_B}(\gamma-1) \left[\frac{\rho_A}{\rho_B}(\gamma-3) + (3\gamma-1) \right]} - (\gamma+1) \frac{\rho_A}{\rho_B}}{\left(\gamma-1 - 2 \frac{\rho_A}{\rho_B} \right)}. \quad (7)$$

This equation has the correct limiting behavior, i.e., when $\rho_B \rightarrow \infty$, $(\rho_A/\rho_B) = 0$ and the reflected particle speed has stagnated $(u/u_1) \rightarrow 0$. In the limit where $(\rho_A/\rho_B) = 1$, there is no contact discontinuity, and the flow is not impeded, $(u/u_1) = 1$. For intermediate cases of (ρ_A/ρ_B) , the impeded flow takes on values $0 < (u/u_1) < 1$ and was verified using the HELIOS radiation-hydrodynamics code²¹ with $\gamma = 5/3$ gases for both region A and region B, and transport physics (radiation and conduction) turned off.

Plotted in Fig. 5(b) are the analytic results for reflected particle speed, normalized to the incident particle speed, and reflected pressure, normalized to the incident pressure, for $\gamma = 5/3$. Other parameters, such as reflected shock density and temperature, can be obtained using these results in the shock jump equations. For $\gamma = 7/5$, the maximum reflected pressure $P_R/P_1 = (3\gamma - 1)/(\gamma - 1) = 8$. The impeded flow (u_R/u_1) has the same endpoints, with different behaviors for intermediate (ρ_A/ρ_B) .

B. Adiabatic compression of foam cushion

After the shock initially passes through the foam cushion and collides with the inner shell, the foam has a relatively high adiabat. The foam continues to be compressed by the outer shell travelling inward, and the outer shell begins to decelerate and compress when the outward going reflected shock reaches the foam/outer-shell interface. Shown in Fig. 6 is the foam average pressure versus time from around shock collision for a HELIOS calculation of a fall-line optimized design. This drive pressure P_D in the foam follows an adiabatic compression, $P_D V^\gamma \sim P_D/\rho^\gamma \sim \text{constant}$, from the time of shock collision with the inner shell until the shock breaks out of the inner shell and reflects an outward going rarefaction wave. For this calculation, the volume V is defined as the annular volume between the outer shell and the inner shell, including the tamper material, and an adiabatic index $\gamma \sim 1.5$ matches this calculation well. The foam pressure plateaus at several Gbar.

As will be described in Sec. IV C, the foam acts as a pressure reservoir that accelerates or drives the inner shell radially inward. Since the inner shell acceleration is proportional to drive pressure P_D , the inner shell velocity will vary as $U \sim \sqrt{P_D}$. As mentioned previously, the sound speed in the foam after shock passage ~ 200 km/s is comparable to the outer shell implosion speed. This allows pressure perturbations to be smoothed to some degree during foam compression and inner shell acceleration. Symmetry

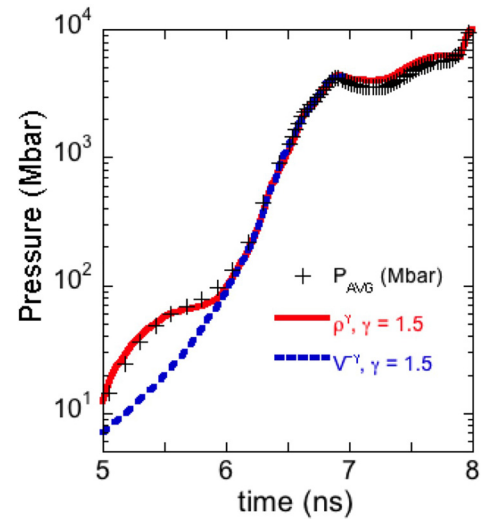


FIG. 6. Average pressure versus time of the foam cushion from the fall-line optimized design, shown as points from 1-D HELIOS. Curves of average foam density (solid red) and foam volume (dashed blue) are plotted, indicating the foam pressure is adiabatic after initial shock passage.

requirements for double shells are beyond the scope of this present paper and will be discussed in future publications.

C. Inner shell kinetic energy: Pressure drive approach

One approach to estimate the kinetic energy of the inner shell is to treat it as a thin shell of initial radius R_0 and mass M_S , while applying a constant external drive pressure P_D . Initially, we ignore the presence of any interior gas, and the acceleration at a radius r is simply

$$a(r) = -4\pi \frac{P_D}{M_S} r^2.$$

Knowing that $a = dU/dt = (dU/dr)(dr/dt) = U(dU/dr)$, we integrate both sides to obtain

$$\begin{aligned} \int a(r) dr &= \int U dU = \frac{1}{2} U^2, \\ KE &= \frac{1}{2} M_S U^2 = -4\pi P_D \int_{R_0}^{R_0/C_R} r^2 dr, \\ KE[C_R] &= +\frac{4}{3} \pi P_D R_0^3 \left(\frac{C_R^3 - 1}{C_R^3} \right), \end{aligned} \quad (8)$$

where the convergence ratio of the inner shell is $C_R = R_0/r$. The maximum possible velocity of the shell, without interior gas, is simply

$$U_{max} = \sqrt{\frac{2KE_{max}}{M_S}} = \sqrt{\frac{8\pi P_D}{3 M_S}} R_0^{3/2}. \quad (9)$$

Before including the effects of the interior gas, we can estimate the required drive pressure P_D for a desired kinetic energy or implosion velocity.¹² Consider an inner shell with finite thickness Δ such that the shell aspect ratio is $A_0 = R_0/\Delta \gg 1$. The shell mass can be approximated as $M_S \approx 4\pi R_0^2 \Delta \rho_S$. Assuming $C_R \gg 1$, the specific kinetic energy of the shell is

$$U^2/2 \approx \frac{P_D 4/3 \pi R_0^3}{4\pi R_0^2 \Delta \rho_S} = P_D A_0 / (3\rho_S),$$

and the required pressure is then

$$P_D = 3\rho_S U^2 / (2A_0). \quad (10)$$

Now, suppose the shell with initial density ρ_S is filled with a gas at an initial density ρ_0 at an initial radius R_0 , such as the inner shell of a double shell. To good approximation, the foam is compressed to a pressure P_D that is external to the inner shell and roughly constant during the acceleration phase. After shock breakout into the gas, the shell will accelerate inward

$$a = -\frac{1}{\rho} \frac{dP}{dr}$$

until the pressure of the gas is greater than or equal to the external drive pressure, i.e., $dP/dr \sim 0$ when $P_D \leq P_F$. Assuming adiabatic compression of the gas

$$\frac{P_F}{\rho_F^\gamma} = \frac{P_i}{\rho_i^\gamma},$$

where P_F and ρ_F are the compressed gas pressure and density at the maximum kinetic energy, and P_i and ρ_i are the initial gas pressure and density set by an initial shock in the gas. The work done on the gas by the inward accelerating shell at an initial pressure P_i is

$$W_g = \int_{V_0}^{V_F} P_i \left(\frac{V_0^\gamma}{V^\gamma} \right) dV = \frac{P_i V_0^\gamma}{1-\gamma} [V_F^{1-\gamma} - V_0^{1-\gamma}] \quad (11)$$

with adiabatic index γ , and the spherical volumes are $V_0 = \frac{4}{3}\pi R_0^3$, $V_F = \frac{4}{3}\pi \left(\frac{R_0}{C_R} \right)^3$.

Assuming $\gamma = 5/3$ and substituting for the spherical volumes, we arrive at

$$W_g = -2\pi P_i R_0^3 [C_R^2 - 1]. \quad (12)$$

The kinetic energy of the shell, accounting for only the work done by the shell on the gas during its acceleration, is then

$$KE[C_R] = \frac{4}{3} \pi P_D R_0^3 \left(\frac{C_R^3 - 1}{C_R^3} \right) - 2\pi P_i R_0^3 (C_R^2 - 1). \quad (13)$$

The external drive pressure P_D determines the shocked particle speed in an actual finite-thickness shell, which after it releases into the gas sets the initial pressure of the gas P_i during shell acceleration, such that $P_i = 4P_D[(\gamma+1)/(\gamma_S+1)](\rho_0/\rho_S)$, where we use γ and γ_S to account for the adiabatic indices of the gas and shell separately. A derivation of the initial gas pressure P_i after shock release is given in [Appendix B](#). The dynamics of this are complex: the initial shock release from the shell into the gas drives an inward shock, and an outward rarefaction wave. When the rarefaction wave encounters the high drive pressure external to the shell, a compression wave is reflected inward, accelerating the shell further, which also drives a second, stronger shock into the gas. Further shell acceleration can occur as the shock continues to reverberate within the shell. The timing of these shocks, rarefactions, and reflected shocks will depend on the shell thickness Δ , initial gas radius R_0 , and how much the shell has accelerated during these times, as well as the adiabatic indices of the shell and gas. In addition, the initial shock in the gas has not fully traversed the gas when the shell begins its acceleration. In the spirit of simplicity of the thin-shell approximation, we estimate that the initial pressure in the gas still scales as the product of the drive pressure and the ratio of the gas and shell densities but with a lower coefficient, $P_i \approx P_D(\rho_0/2\rho_S)$, based on numerous radiation-hydrodynamic simulations. We can then write

$$KE[C_R] \approx 2\pi P_D R_0^3 \left[\frac{2}{3} \left(\frac{C_R^3 - 1}{C_R^3} \right) - \left(\frac{\rho_0}{2\rho_S} \right) (C_R^2 - 1) \right]. \quad (14)$$

Shown in [Fig. 7](#) is the kinetic energy of the inner shell of double shell capsules from HELIOS simulations.

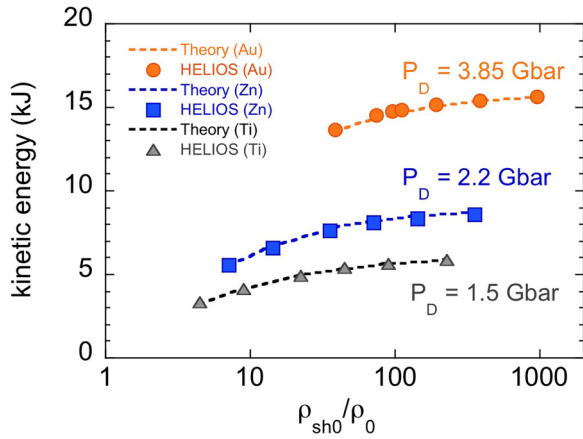


FIG. 7. Plots of inner shell kinetic energy versus ratio of shell density to D-T fill density from 1-D HELIOS simulations for a Au pusher (circles), a Zn pusher (squares), and a Ti pusher (triangles). The dashed lines are theory from Eq. (14) at a fixed drive pressure for each case.

Calculations were performed for Au (19.3 g/cm^3), Zn (7.14 g/cm^3), and Ti (4.51 g/cm^3) inner shells with fixed gas radius $R_0 = 215\text{-}\mu\text{m}$ and fixed inner shell thickness $\Delta = 40\text{-}\mu\text{m}$, with fixed foam cushion (CH at 35 mg/cm^3), Al outer shell ($R = 1.11\text{-mm}$, $175\text{-}\mu\text{m}$ thick), and radiation drive temperature. The D-T initial fill density was varied between $\rho_0 = 0.02$ and 1.0 g/cm^3 , and alpha deposition was turned off. For the analytic estimates, the drive pressure P_D was found by taking the average pressure between inward shock break out into the gas and outward rarefaction release from the shell into the foam, and assuming it is constant during the inner shell acceleration phase. The estimated inner shell kinetic energy from Eq. (14) agrees quite well with that found in HELIOS simulations.

In these simulations, we fixed the CH foam density at 0.035 g/cm^3 , which is the lowest density CH foam that can currently be produced, machined, and assembled within a double shell. With lower density foam, slightly more inner shell kinetic energy can be obtained since less internal energy is going into the foam, but the faster travelling shock in the foam puts the inner shell and fuel on a higher adiabat, making them less compressible during stagnation. Further simulations and theoretical work are required to better understand the optimum foam density, as well as possible benefits in using lower density foams or foams with high-Z dopants to tailor their compression.

D. Optimum inner shell thicknesses

The overly simplistic pressure-driven thin-shell model above ignores the shell thickness, which effectively determines what drive pressures are achievable. When the main shock collides with the inner shell, a transmitted shock propagates inward toward the D-T gas, and a reflected shock propagates outward toward the incoming outer shell. When the transmitted shock reaches the shell-gas interface, a shock is transmitted inward into the gas, and a rarefaction wave propagates outward toward the shell-foam interface. When the rarefaction wave reaches this interface, the pressure begins to drop in the foam. The shock driven by pressure P_D

transits a high-Z shell of thickness Δ , density ρ_S , and adiabatic index γ_S with shock speed $u_S \approx \sqrt{P_D(\gamma_S + 1)/2\rho_S}$, and the rarefaction wave transits back through the compressed shell at the sound speed $c_S \approx \sqrt{\gamma_S P_D(\gamma_S - 1)/\rho_S(\gamma_S + 1)}$. The total duration for the shock through the uncompressed shell and rarefaction wave through the compressed shell is $\tau \approx \Delta(\sqrt{\gamma_S - 1} + \sqrt{2})/(\sqrt{(\gamma_S + 1)P_D/\rho_S})$. For a drive pressure of $P_D = 1.2 \text{ Gbar}$, $\rho_S = 19.3 \text{ g/cm}^3$, $\gamma_S = 1.5$, and shell thickness $\Delta = 50\text{-}\mu\text{m}$, the total transit time for the shock and rarefaction waves is $\tau = 0.85 \text{ ns}$. Appendix B contains a fit of the adiabatic index γ_S for a Au shell in the strong shock limit in the range 0.2–10 Gbar for useful estimates of the shell EOS during the acceleration phase.

The reflected shock propagates outward towards the outer shell, and when it collides with the outer shell, the shell begins to compress.²² When this shock reaches the ablation front region of the outer shell, a rarefaction wave is launched inward, decompressing the outer shell. Simulations indicate that for a fixed outer shell thickness and radiation drive, and a fixed outer radius of the inner shell, the optimum kinetic energy transfer occurs when the release from the inner shell to the foam coincides with the initial release of the outer shell. In Fig. 8(a), we show a contour plot of the logarithmic derivative of the density, $(1/\rho)\partial\rho/\partial r$, versus Lagrangian index and time for a HELIOS simulation with a fixed outer Al shell and radiation drive, and an inner shell external radius $R_{\text{ext}} = 300\text{-}\mu\text{m}$ and thickness $\Delta = 52\text{-}\mu\text{m}$. The times for release from the inner shell into the foam and initial release of the reflected shock at the outer shell coincide at 6.8 ns. In contrast, a simulation for a thinner inner shell ($\Delta = 10\text{-}\mu\text{m}$) is shown in Fig. 8(b). Here, the reflected shock reaches the outer shell at the same time (6.8 ns) as in Fig. 8(a) since R_{ext} is the same, but the release from the inner shell into the foam occurs earlier since the thickness Δ is smaller, thus the drive pressure drops. The kinetic energy for the thicker inner shell shown in Fig. 8(a) is 21.5 kJ, compared to 11.7 kJ for the thin shell case shown in Fig. 8(b). As further comparison, a plot of the pressure versus time at the outer zone of the inner shell is shown in Fig. 9 for the thin and thick shell cases. Shock collision with the inner shell occurs at 6.15-ns for both cases. The pressure is identical through initial shock and release for the thin and thick shell, and drops upon release at about 6.25 ns for the $\Delta = 10\text{-}\mu\text{m}$ case, resulting in $P_D \sim 1 \text{ Gbar}$, and release occurs at around 6.8 ns for the $\Delta = 52\text{-}\mu\text{m}$ case, resulting in $P_D \sim 3 \text{ Gbar}$. Decompression of the outer shell after the reflected shock reaches the ablation front occurs at 6.8 ns, coinciding with the release from the inner shell into the foam, shown as the average density of the outer shell in Fig. 9. Several other simulations were performed with fixed outer shell and radiation drive, and varying R_{ext} and Δ , in the limit of low D-T fuel density, and the inner shell kinetic energy transfer efficiency, normalized to the outer shell kinetic energy, is shown as the points in Fig. 10. The inner shell kinetic energy for fixed R_{ext} is optimized at a thickness Δ when the release coincides between inner and outer shells. A smaller radius inner shell R_{ext} requires a thicker shell Δ compared to a

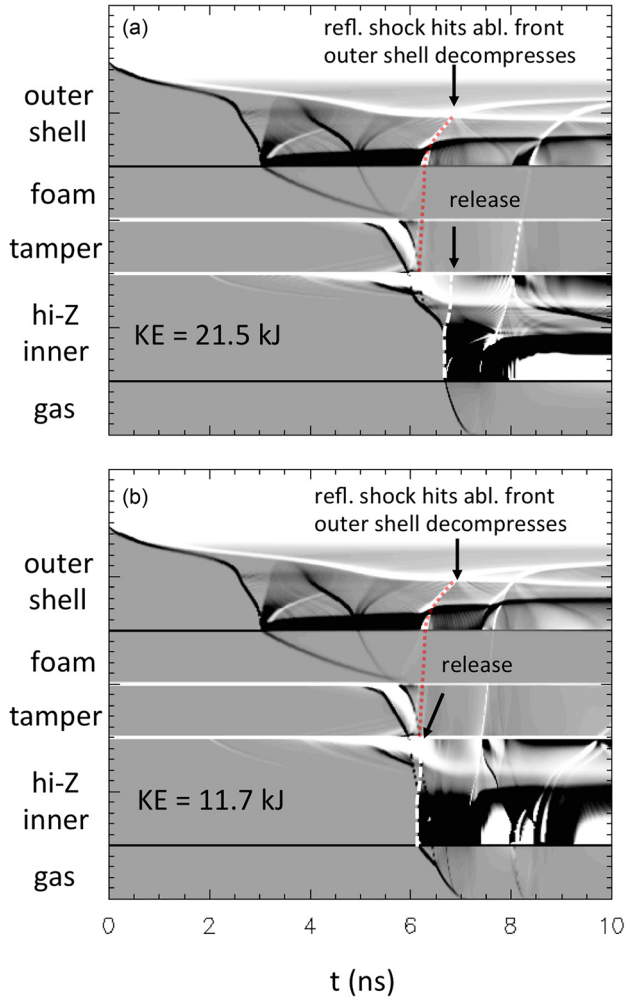


FIG. 8. Contour plots of the logarithmic derivative of the density versus Lagrangian index and time for fixed inner shell external radius of 300- μm and thickness (a) 52- μm and (b) 10- μm . The main shock in the foam collides with the inner shell at the same time, and propagates outward to collide with the outer shell at the same time. The shock and rarefaction transit occurs sooner for the thinner shell than the thicker shell, and the foam begins to decompress before the outer shell has reached maximum compression for the thin shell case, resulting in less kinetic energy transfer.

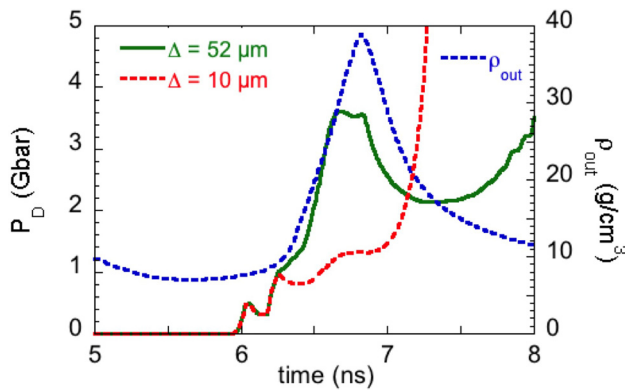


FIG. 9. Plots of inner shell drive pressure versus time for the thick shell (solid green) and thin shell (dashed red). Both pressure curves are identical until ~ 6.25 ns when the shock and rarefaction transit occurs for the thin (10- μm) shell. The dashed blue curve is the outer shell average density. It reaches peak compression at the same time as the drive pressure begins to drop for the thick inner shell. Maximum kinetic energy transfer occurs for the inner shell when these two coincide.

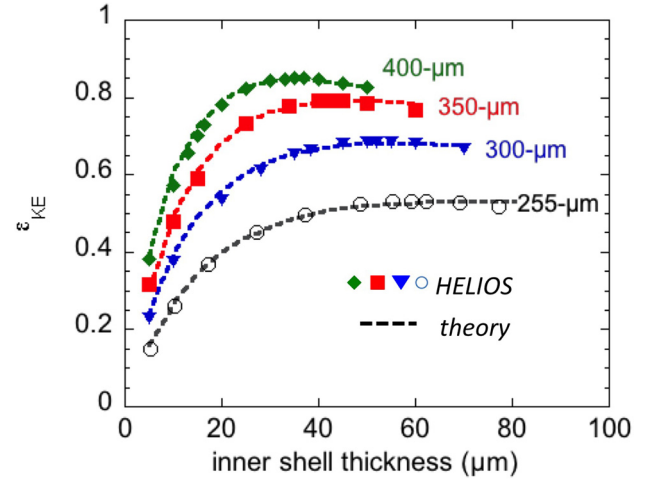


FIG. 10. Kinetic energy transfer efficiency from the outer to inner shell from 1-D HELIOS simulations versus inner shell thickness at varying radii, shown as points. Dashed lines are from partially inelastic collision theory, Eq. (15).

larger radius inner shell due to spherical convergence effects causing higher pressures, requiring a thicker shell to match the release times for inner and outer shells. Larger radii inner shells have higher kinetic energy transfer efficiencies than smaller radii inner shells. While the available drive pressure is higher for smaller radii inner shells due to spherical convergence of the main shock and larger compression of the foam, less kinetic energy is actually transferred since $KE \sim P_D R_0^3$.

E. Inner shell kinetic energy: Collision approach

Despite the complexity of multiple interfaces and reflecting shock and release waves between them, a simple 1-D collision approach describes the kinetic energy transfer between the inner shell and outer shell quite well. Consider the 1-D collision kinematics of a particle of mass m_1 and velocity v_1 colliding head on with an initially stationary particle of mass m_2 and velocity $v_2 = 0$. We allow for a partially inelastic collision between the two particles with a coefficient of restitution $-1 \leq C_{res} \leq 1$, where $C_{res} = (v'_2 - v'_1)/(v_1 - v_2)$, and the primed quantities refer to after the collision. A coefficient of restitution $C_{res} = 1$ represents an ideal elastic collision. The kinetic energy transfer efficiency from particle 1 to particle 2 is then

$$\varepsilon_{KE} = \frac{(1 + C_{res})^2}{(1 + m_2/m_1)^2} \left(\frac{m_2}{m_1} \right). \quad (15)$$

For the case of $C_{res} = 1$ and $m_2 = m_1$, it yields $\varepsilon_{KE} = 1$ as expected. We use Eq. (15) as a functional form to fit to the simulation data in Fig. 10, which are shown as the dashed lines. The coefficient of restitution found for these and other simulations with smaller R_{ext} is shown in Fig. 11. For sufficiently large inner shells, the collision is nearly elastic, $C_{res} \sim 1$, and most of the energy is transferred between inner and outer shells. The inner shell mass which gives the most kinetic energy transfer (thickness where release between inner and outer coincide, Sec. IVD) is nearly mass matched

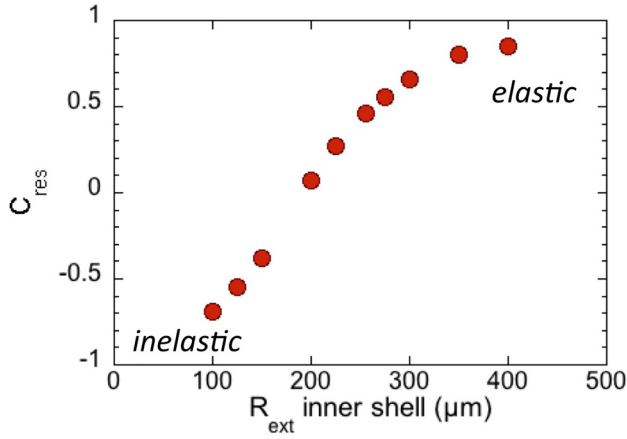


FIG. 11. Coefficient of restitution from Eq. (15) versus inner shell radius. Larger radii inner shells behave more like elastic collisions than smaller radii inner shells.

with the outer shell remaining mass, $m_2 \sim m_1$. For smaller radii inner shells, the coefficient of restitution decreases, as shown in Fig. 11, such that the collision becomes more inelastic. For smaller radii inner shells R_{ext} , the outer shell is compressed further than for larger R_{ext} , meaning more of the kinetic energy is turned into internal energy in the outer shell, rather than stored as a pressure reservoir in the foam. Slightly smaller m_1 than the actual mass remaining in the outer shell are required to fit the simulation points for smaller R_{ext} . As a point of reference, for the calculations we show with the Al outer shell external radius of 1.11-mm and thickness 175- μm , the outer shell reaches its maximum kinetic energy after the laser drive turns off at 6.0 ns when the outer-shell/foam interface has converged to a radius slightly more than $\sim 400\text{-}\mu\text{m}$, which is the largest inner shell we considered. This was to avoid the complexity of considering kinetic energy transfer to the inner shell while the outer shell is still accelerating.

V. COMPRESSION AND STAGNATION

At the end of the acceleration phase, when the inner shell has reached its maximum kinetic energy, $\partial P/\partial r \sim 0$, the initial pressure of the D-T fuel is about equal to the drive pressure on the inner shell, $P_0 \sim P_D$. This also coincides with when the reflected shock in the D-T gas collides with the inner shell. The shell is compressed by the outward going shock as it also does PdV work on the gas. After the initial shock transit and reflection, both the gas and the shell are on an initial adiabat, and the remaining compression during the deceleration phase can be considered quasi-adiabatic. While sophisticated models can be developed to more accurately describe the deceleration phase for a thick shell,²² it is instructive to consider a simple quasi-static adiabatic model for scaling purposes.

Consider a decelerating inner shell of mass M_S with initial inward velocity U . Assume that the shell initial pressure is identical to the initial gas pressure $P_0 \sim P_D$, and the initial volumes for the shell and gas are V_{S0} and V_{DT0} , with adiabatic indices γ_S and γ . At stagnation, assume an isobaric configuration between the shell and gas with final pressure P_F

and that all of the kinetic energy is converted into internal energy of the shell and gas. The energy equation is then

$$\frac{1}{2}M_S U^2 + M_S \epsilon_{S0} + M_{DT} \epsilon_{DT0} = M_S \epsilon_{SF} + M_{DT} \epsilon_{DTF}, \quad (16)$$

where the subscripts (0, F) refer to initial and final states. Since the specific internal energies can be expressed as $\epsilon = P/\rho(\gamma - 1) = PV/M(\gamma - 1)$, we use the adiabatic expression $P_0 V_0^\gamma = P_F V_F^\gamma$ and rewrite the energy equation as

$$\begin{aligned} \frac{1}{2}M_S U^2 = & \frac{P_0 V_{S0}}{\gamma_S - 1} \left[\left(\frac{P_F}{P_0} \right)^{\frac{\gamma_S - 1}{\gamma_S}} - 1 \right] \\ & + \frac{P_0 V_{DT0}}{\gamma - 1} \left[\left(\frac{P_F}{P_0} \right)^{\frac{\gamma - 1}{\gamma}} - 1 \right]. \end{aligned} \quad (17)$$

For adiabatic indices with a similar value, the partition in internal energy between the fuel and shell at stagnation is determined mostly by the initial volumes of the D-T fuel and shell at the beginning of the deceleration phase, V_{DT0} and V_{S0} . As an example, for a D-T gas radius $R_d \approx 50\text{-}\mu\text{m}$ and shell thickness $\Delta_d \approx 40\text{-}\mu\text{m}$, the ratio of initial gas to shell volume is $V_{DT0}/V_{S0} \approx 1/5$, or roughly 1/5 of the kinetic energy becomes internal energy of the gas. To be useful, one has to make assumptions about the initial internal energies or volumes of the shell and gas at the start of the deceleration phase. In addition, this simple model assumes the entire shell is compressing adiabatically. A more complete dynamic model, such as described by Betti *et al.* for thick shells,²² indicates that the inner portion of the shell in contact with the D-T gas is incompressible after the reflected shock passage, and the remaining unshocked outer region of the shell remains compressible.

Examining initial and final stagnation pressures and temperatures from 1-D HELIOS simulations of double shells, the adiabatic index for the D-T behaves more like $\gamma \sim 1.5$, rather than $\gamma = 5/3$, which partly reflects the increasing role of radiation in the internal energy and pressure, but more likely the conduction and radiation losses from the gas into the wall. An adiabatic index of 5/3 overestimates the pressure and temperature of the D-T gas with this simple model.

As an initial estimate, we consider some parameters from optimized 1-D HYDRA simulations: a yield-optimized capsule and a fall-line optimized capsule. Both have an Al outer shell of outer radius 1.11-mm and use the same radiation drive which peaks at $\sim 300\text{ eV}$. For these comparisons, we turn α -deposition off to estimate the stagnated conditions. Further details of these designs will be discussed later in Sec. VIII. Key parameters for each design are provided in Table II. Both designs use a $\Delta = 40\text{-}\mu\text{m}$ thick tungsten shell, which we model in HELIOS using a Au shell.

For the yield-optimized and fall-line optimized designs, the initial internal energy of the D-T fuel is $\epsilon_{DT0} = 1.0\text{ kJ}$ and 0.75 kJ , respectively, with initial D-T fuel densities of 0.24 and 0.20 g/cm^3 , respectively. We find a shell adiabatic index $\gamma_S = 1.285$ that works best for both capsules. The yield-optimized design has a slightly larger inner shell and larger D-T fuel mass, and the inner shell kinetic energy is larger, as

TABLE II. Key design parameters for yield-optimized and fall-line optimized designs.

	Yield optimized	Fall-line optimized
R_0	265 μm	215 μm
M_{DT}	18.71 μg	8.32 μg
M_S	789 μg	537 μg
KE	20 kJ	15 kJ
IE_{DT}	6.2 kJ	3.8 kJ
IE/KE	0.31	0.24
P	480 Gbar	1067 Gbar
P_0 model input	2.5 Gbar	10 Gbar
P_F model	500 Gbar	1100 Gbar
IE/KE model	0.29	0.23
SIE/KE model	0.016 μg^{-1}	0.029 μg^{-1}

expected from our estimates in Sec. IV. The initial pressure of the D-T fuel and shell at peak kinetic energy is about $P_0 = 2.5$ Gbar and stagnates at 480 Gbar in the HYDRA simulation. Using the parameters from the adiabatic model, we find $P_F = 500$ Gbar, in very good agreement with these results. This is roughly a final convergence, from onset of deceleration to stagnation, of $R/R_F \approx (P_F/P_0)^{1/3\gamma}$ or about 3.25.

The fall-line optimized design has a smaller initial fuel radius and smaller fuel mass, and the inner shell kinetic energy is smaller than for the yield-optimized design, as expected for the smaller initial fuel radius R_0 . However, it is important to realize that one wants to ultimately optimize for specific internal energy of the fuel, and not necessarily shell kinetic energy. The initial pressure of the D-T fuel for this design at peak kinetic energy is 4 times larger than for the yield-optimized design, $P_0 = 10$ Gbar, due to spherical convergence effects of both the main initial shock and the higher available drive pressure since the outer shell has further to travel and compresses the foam to higher pressures. At stagnation, the 1-D HYDRA calculations indicate a fuel pressure of 1067 Gbar. Using the parameters from the adiabatic model, we find $P_F = 1100$ Gbar, in good agreement with the calculations. This is roughly a final convergence of $R/R_F \approx 2.85$. The efficiency of transfer from kinetic energy to D-T internal energy is $IE/KE \sim 0.29$ and 0.23 , respectively, from the adiabatic model for the yield-optimized and fall-line optimized designs, in good agreement with the 1-D HYDRA calculations in Table II. However, one wants to optimize specific internal energy to obtain robust burn, which we discuss next in Sec. VI. The specific fuel internal energy efficiency from shell kinetic energy is $SIE/KE = 0.016 \mu\text{g}^{-1}$ and $0.029 \mu\text{g}^{-1}$ for the yield-optimized and fall-line optimized designs. While shell KE is higher for the large fuel radius R_0 and results in more fuel internal energy, the fuel mass scales as $\sim R_0^3$ at fixed fuel density, so the specific internal energy is higher for the smaller-radius fall-line optimized design.

It is worth noting that both designs have a final convergence, from onset of deceleration phase to stagnation, of $R/R_F \sim 3$, meaning that the pressure amplification during this phase is roughly the same for these designs. Therefore, the design with smaller fuel radius starts at a larger initial pressure due to spherical convergence effects and has a higher stagnation pressure and specific internal energy than

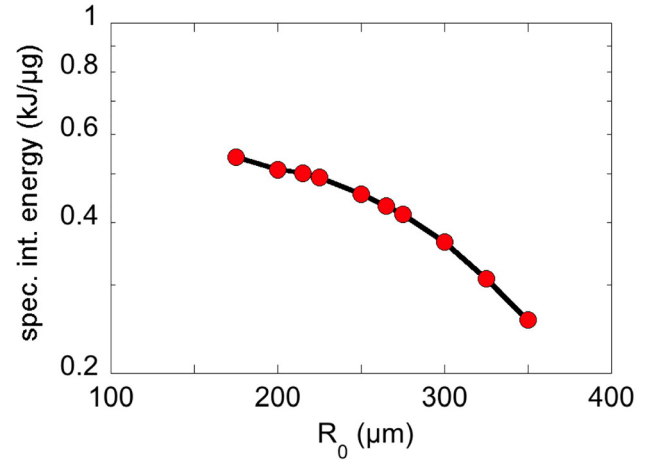


FIG. 12. Specific internal energy of D-T fuel at fixed initial density $\rho_0 = 0.2 \text{ g/cm}^3$ versus inner shell radius, from 1-D HELIOS simulations, alpha-deposition off. While larger radii inner shells obtain more kinetic energy, the D-T fuel mass increases as R^3 . For a fixed radiation drive temperature and outer shell radius, the D-T specific internal energy at stagnation increases for smaller radii inner shells. Further increases of specific internal energy with smaller inner shell radii diminish since the inner shell kinetic energy decreases faster.

those with larger radii. Figure 12 shows a plot of 1-D HELIOS simulations with the same Al outer shell and radiation drive as for the fall-line and yield-optimized designs. The initial D-T fuel density was fixed at $\rho_0 = 0.2 \text{ g/cm}^3$ and the Au inner shell thickness fixed at $\Delta = 40\text{-}\mu\text{m}$, and the initial fuel radius was varied between $R_0 = 175$ and $350 \mu\text{m}$. The specific internal energy (SIE) of the D-T fuel at stagnation, with α -deposition off, is plotted versus R_0 . The SIE increases quadratically with decreasing R_0 , but provides diminishing returns for $R_0 < 200\text{-}\mu\text{m}$. One also wants sufficiently large fuel areal density $\rho R_{\text{DT}} > 0.3 \text{ g/cm}^2$ for efficient α -heating and robust burn, which we discuss next in Sec. VI.

VI. ROBUST BURN MODEL

In 1-D radiation-hydrodynamic simulations of double shell targets with α -deposition turned on, the dominant loss mechanism is the PdV work of the hot D-T plasma pushing outward on the shell, expanding and cooling the hot spot. In simulations of marginally igniting capsules, the inequality in Eq. (18) appears to be confirmed. Other losses—radiation and thermal conduction—are driven by temperature gradients from fuel to shell, and tend to require that the fuel be hot enough that ignition by Eq. (18) has already occurred. In this regard, these other losses are perhaps more applicable to quantifying capsule performance. At minimum, we want the majority of burn and useful yield to occur before the hot spot disassembles, which sets a requirement on the fuel ρR and stagnation temperature. We define an ignition temperature by requiring the specific α -heating power to exceed specific power losses due to PdV work

$$\dot{q}_\alpha + \dot{q}_{PdV} > 0, \quad (18)$$

where

$$\dot{q}_\alpha = \frac{n_D n_T \langle \sigma v \rangle Q V_{DT}}{M_{DT}} \rightarrow \frac{\text{energy}}{\text{mass} \cdot \text{time}} \quad (19)$$

and n_D and n_T are the deuteron and triton densities, $\langle \sigma v \rangle$ is the fusion reactivity averaged over a Maxwellian ion velocity distribution, and Q is the alpha energy deposited in the D-T plasma. We estimate the specific PdV power loss as

$$\dot{q}_{PdV} = \frac{P}{M_{DT}} \frac{dV}{dt} \approx \frac{P}{M_{DT}} \left(\frac{Ac_S}{f_{tamp}} \right), \quad (20)$$

where A is the surface area of the hot spot, perhaps with low-mode asymmetry, and $c_S = \sqrt{\gamma P / \rho}$ is the sound speed in the D-T plasma, and we introduce an expansion tamping factor f_{tamp} which accounts for tamped expansion due to the shell. We can parameterize the D-T fusion reactivity as a power law of ion temperature in our regime, $\langle \sigma v \rangle \approx 2.2 \times 10^{-20} T^4 \text{ cm}^3/\text{s}$, where the ion temperature is in the range $2.5 < T < 5.5 \text{ keV}$. Noting that $c_S \sim P^{1/2}$ and $P \sim T$ in Eq. (20), the PdV specific power loss term scales as $\dot{q}_{PdV} \sim T^{1.5}$.

For an ideal sphere of D-T plasma, $A/V = 3/R$. We define $A/V \equiv 3/R_*$, where $A/V > 3/R$ as the hot spot distorts. Noting that $P = T(n_D + n_T + n_e)$ and assuming $n_D = n_T$, we find $P = 4Tn_D$. Combining these results and Eqs. (18) and (19) into Eq. (20), we have

$$\langle \sigma v \rangle Q > \frac{24\gamma^{1/2} T^{3/2}}{\rho R_* f_{tamp}} \left(\frac{\bar{A}_W}{N_A} \right)^{1/2}, \quad (21)$$

where $\bar{A}_W = 2.5$ is the average atomic weight for a 50/50 D-T plasma mixture and N_A is Avogadro's number. Assuming the alpha-deposited energy is $Q = \hat{Q} \cdot 3.5 \text{ MeV}$, where \hat{Q} is the fraction of alphas absorbed, $0 < \hat{Q} < 1$, and plugging in numerical values, we arrive at

$$T > \frac{4}{(\rho R_* f_{tamp} \hat{Q})^{0.4}} [\text{keV}], \quad (22)$$

which is valid in the range $2.5 < T < 5.5 \text{ keV}$. At this point, it is instructive to make a simple estimate. For $\rho R_* = 0.3 \text{ g/cm}^2$, $f_{tamp} = 3.3$, and $\hat{Q} \sim 1$, then the minimum stagnation temperature where α -heating exceeds PdV losses is $\sim 4 \text{ keV}$. This is quite higher than the temperature required for α -heating to exceed radiation losses in a high-Z shell, $T \sim 2.5 \text{ keV}$, see, for example, Molvig *et al.*,²³ and roughly where the ion temperature starts to deviate between the burn-on and burn-off cases in full double shell simulations.

For the α -deposition fraction \hat{Q} , the fraction of energy deposited is estimated with alpha range using the method in Krokhin and Romanov²⁴

$$\hat{Q} = \frac{3}{2} \tau - \frac{4}{5} \tau^2, \quad \text{for } \tau < 0.5, \quad (23a)$$

$$\hat{Q} = 1 - \frac{1}{4\tau} + \frac{1}{160\tau^3}, \quad \text{for } \tau \geq 0.5, \quad (23b)$$

where $\tau = R/\lambda_K$; here, R is the fuel hot spot radius and λ_K is the alpha range, and the alpha range is a fit from

Kirkpatrick and Wheeler²⁵ based on work by Cooper and Evans²⁶

$$\rho \lambda_K \approx 0.03 T_e [1 - 0.24 \log(1 + T_e)] \times \left[1 + 0.37 \log \left(\frac{1 + \rho}{1 + 0.01 T_e^2} \right) \right]. \quad (24)$$

As the pressure in the D-T rapidly increases during ignition, it launches an outward going shock wave into the dense, high-Z pusher. This is analogous to a shock tube, where a high pressure “drive gas” launches a shock wave into a lower pressure “test gas.” While the shock travels rapidly through the “test gas,” the “drive gas” expands at the contact discontinuity speed. In the case of a double shell, the hot spot cannot expand faster than the motion of the contact discontinuity, i.e., the gas/shell interface. The speed of the contact discontinuity with respect to the drive gas sound speed, u/c_s , is derived analytically by Zel'dovich and Raizer,²⁷ and is given by

$$\frac{u}{c_s} = \frac{2}{\gamma - 1} \left\{ 1 - \left[\frac{\gamma(\gamma_c + 1)}{2} \left(\frac{\rho_c}{\rho_{gas}} \right) \left(\frac{u}{c_s} \right)^2 \right]^{\frac{\gamma-1}{2\gamma}} \right\}, \quad (25)$$

where γ and γ_c are the adiabatic indices of the gas and the contact discontinuity, and ρ_c/ρ_{gas} is the density ratio of the shell and gas at the contact discontinuity. The expansion tamping factor is then $f_{tamp} = c_s/u$. Using $\gamma = 5/3$ for the hot D-T gas and $\gamma_c \sim 3$ for the contact part of the shell, a convenient fit to the tamping factor from Eq. (25) is $f_{tamp} \approx 2(\rho_{gas}/\rho_c)^{-0.4}$, which gives a tamping factor $f_{tamp} \sim 3$ – 4 for typical conditions of $\rho_{gas} \sim 150$ – 300 g/cm^3 and $\rho_c \sim 1000 \text{ g/cm}^3$.

This simple model for the tamping factor should be applicable until the outward propagating shock breaks out into the tamper. For heavily tamped designs (large pusher mass), this time scale is expected to be longer than the burn duration. As an example, for the fall line design, the outward shock velocity is $\sim 470 \mu\text{m/ns}$ and takes $\sim 90 \text{ ps}$ (after bang time) to traverse the pusher. However, the burn width is only $\sim 40 \text{ ps}$ for this design, and thus burn is completely finished before the shock breaks out. Thus, the tamping factor in Eq. (25) should provide a reasonable description throughout the burn, at least for the most interesting limit of heavily tamped designs (large pusher mass).

Significant burn fractions are observed for all simulations in which the ignition condition Eq. (22) is satisfied. As expected, the observed burn fraction increases with the fuel ρR , but also depends upon the high-Z pusher. However, to make analytic estimates of the burn fraction using the traditional approach^{3,37} requires an understanding of the confinement time (burn duration). For central hot-spot ignition, the confinement time is set by the inward rarefaction wave, which propagates at the sound speed. In a time scale $\sim R/(3c_S)$, this rarefaction passes through the outer dense fuel region and terminates the burn. However, this argument does not apply to double-shells, where the sound crossing time (R/c_S) is a factor of several shorter than the observed burn duration. In this limit, sound waves can bounce around the cavity and equilibrate pressure. During this volumetric burn, the gas interface expands outward by $\sim 30\%$, leading to

a $\sim 2\times$ decrease in gas density, and a reduction in fusion reactivity. During significant burn, the dominant loss term is then radiation associated with the outward propagating Marshak wave into the high-Z pusher. As burn is initiated, this leads to the ablation of pusher material into the fuel, and a corresponding radiation recompression. Since the radiation temperature is changing rapidly in time, it is difficult to make simple analytic estimates of such time-dependent Marshak waves, e.g., see Ref. 38. Ultimately, the burn duration is determined by this Marshak wave, along with the reduction in reactivity due to depletion and expansion of the fuel. We leave this difficult problem for future work.

VII. MANUFACTURING CONSIDERATIONS

For double shell capsule designs, there is an inherent flexibility in possible choices of materials for the outer shell, foam cushion, high-Z inner shell, and tamper layer. To down select from this potentially vast array of choices, optimization of both physics design goals as well as the ability to fabricate a double shell capsule must be considered simultaneously. For example, for the outer shell, one wants a material with high ablation efficiency and good x-ray preheat shielding for physics design goals, and the ability to machine, polish, and assemble two hemispherical shells around the foam and inner shell assembly.

Table III shows the following outer shell materials we have considered for both physics design goals and manufacturing: Cu-doped Be, pure Al, and Al alloys. We performed 1-D HYDRA simulations for all cases, and used either existing experience with material machining, polishing, and handling, or predictions based on material strength and grain size.

We have discounted the use of CH ablators based on low ablation efficiency, issues with machinability, and the need for a dense shell during the collision phase to optimize energy transfer to the inner shell. We also discounted the use of high-density carbon (HDC) ablators based on machining experience. Our design work with Cu-doped Be ablators (0.2%–0.9% uniformly doped Cu) indicated good ablation efficiency, but insufficient M-band (2–3 keV) preheat shielding, and poor collision efficiency to the inner shell. Previous work with Cu-doped Be indicated that the material had good characteristics for machining and durability during assembly, and could be polished to high surface finish.²⁸

We also considered aluminum for outer shells, ranging from pure Al to commercially available Al alloys. Pure Al is calculated to have good ablation efficiency, excellent x-ray preheat shielding, and good collision efficiency to the inner

shell. However, it is relatively soft, which makes it difficult for machining and handling during assembly. Standard implosion radiography on NIF uses 9-keV Cu He- α backlighters, which works well for CH, Be, and HDC ablators, but would be too opaque for Al-based ablators. Recent work on NIF has demonstrated radiography capability with 16-keV Zr He- α backlighters with a pure Al ablator.²⁹ Alloys, such as Al-6061, have excellent machining and polishing characteristics required for the outer shell but are poor ablators due to the high-Z impurities used to produce the alloy, which radiate away the absorbed x-ray energy. A commercially available material, AlBeMet, was also considered in our designs, which is 83% Be and 17% Al by atomic fraction. While 1-D HYDRA calculations indicated good ablation efficiency, x-ray preheat shielding, and collision efficiency, the material had unknown machining properties, and initial sample characterization obtained from the vendor showed large heterogeneous grains of Al and Be in a binary composite, rather than the Al being fully solved into the Be as an alloy. Our current double shell capsule designs focus on pure Al outer shells, or Al-1100 (99% pure Al) as a backup. Better physics design performance is gained using this ablator, which is traded for increased difficulty in machining and handling.

To maximize kinetic energy transfer from the outer to the inner shell, the foam cushion should be as low density as feasible. This conflicts with manufacturing constraints, where mid to high density foams can be machined to high accuracy. The foam should also have small pore size and be uniform in density throughout the sample. Substantial experience exists in synthesizing, molding, and machining SiO₂ aerogel and CH foams. The lowest densities that are successfully machined to sub-micron accuracy are CH foams at 30–40 mg/cm³, which have been the choice for our current designs. Higher density foams result in a slower main shock, and less kinetic energy transfer from the outer shell to inner shell. Improvements in kinetic energy transfer from outer to inner shell may be gained with reduced foam density. However the faster shock in low density foam can lead to inner shell preheat due to the radiative shock, and the faster shock leads to a higher adiabat for the inner shell and gas, and degraded implosion performance. These design trade-offs require full hydrodynamic simulations to optimize the foam density while also considering the ability to make, machine, and assemble the foam in the capsule.

The high-Z inner shell can be deposited by vapor deposition or electroplating on to a polymer mandrel, which is removed by pyrolysis after the high-Z shell is formed. High

TABLE III. Physics and manufacturing considerations for ablator materials.

	Physics considerations				Manufacturing considerations		
	Ablation efficiency	Preheat shield	Collision efficiency	Diagnose on NIF?	Machinability and durability	High-Z impurities	Surface roughness
0.9% Be/Cu	Excellent	Poor	Poor	Yes	Good	Good	Good
Al-pure	Good	Excellent	Good	Maybe	Fair	Excellent	Good
Al-6061	Poor	Excellent	Good	No	Excellent	Poor	Excellent
AlBeMet	Good	Good	Good	Maybe	Unknown	Good	Unknown

density and high-Z are desirable to achieve high pressure with low convergence, see Sec. II A. Materials that are malleable and ductile, such as Au and Cu, tend to cold weld during vapor deposition on a mandrel, so must be electroplated.³⁰ Our current designs employ a tungsten inner shell, over coated with a beryllium tamper, formed by vapor deposition on a polymer mandrel. Initial research indicates that the inner shell could be graded in density between W and Be³⁰ to help mitigate hydrodynamic instability during acceleration phase.¹¹

VIII. 1-D OPTIMIZED DESIGNS

We focused on two strategies for 1-D optimization: optimization of 1-D yield solely or optimization of both fall-line behavior and 1-D yield. For the latter case, higher 1-D yield is traded for better fall-line performance.¹¹ We used 2-D HYDRA integrated calculations with a 5.75-mm diameter Au hohlraum with a He fill density of 0.03 mg/cm^3 . The hohlraum was 9.43-mm long with a 3.45-mm diameter laser entrance hole (LEH). The laser pulse was a reverse ramp pulse shape with a peak power of 450 TW, 5 ns duration, see Fig. 13. Here, the inner cones are delayed by 0.9 ns as an initial scheme to control P2 symmetry. More recent design work uses a time-dependent cone fraction to balance cone fraction and control P2 and P4.³¹ A 1-D frequency-dependent source (FDS) was generated using the 2-D integrated calculations as input for the 1-D optimization calculations with HYDRA.

The capsule outer shell was an aluminum (Al) ablator with a fixed outer radius of 1.11-mm. The cushion was chosen to be CH foam with a uniform density of 35 mg/cm^3 . The inner shell is $40\text{-}\mu\text{m}$ thick tungsten with a $40\text{-}\mu\text{m}$ thick Be tamper layer between the foam and inner shell. The Be tamper layer prevents outward expansion of the W inner shell due to hard x-ray preheat and also lowers the Atwood number between the low density foam and tungsten shell to mitigate hydrodynamic instabilities at that interface. The fuel is liquid D-T in the range of $0.177\text{--}0.24 \text{ g/cm}^3$, compatible with the current NIF cryogenic target system.

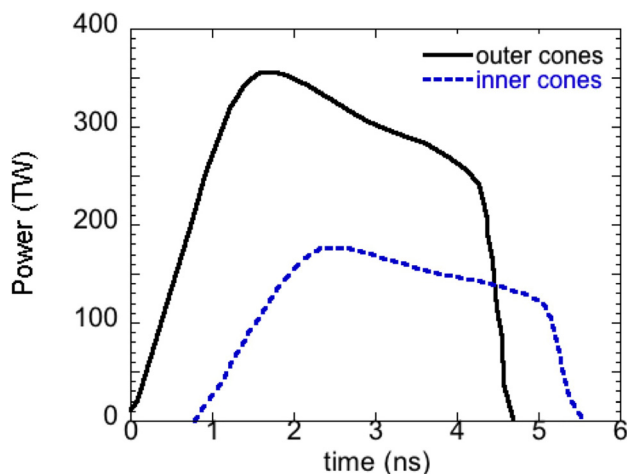


FIG. 13. Outer and inner cone power versus time used in the 2-D HYDRA simulations.

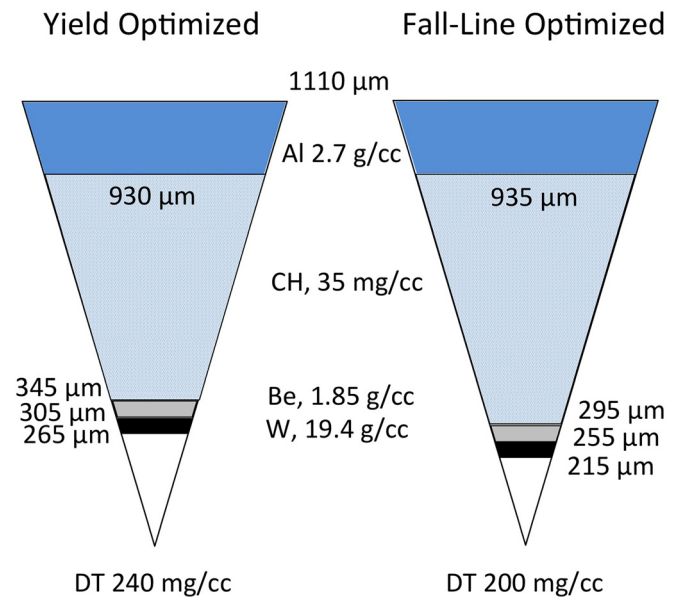


FIG. 14. Pie diagrams of double shell capsules for (a) yield-optimized design and (b) fall-line optimized design.

Pie diagrams of the 1-D yield optimized and fall-line optimized designs are shown in Fig. 14. Both designs have nearly the same outer shell thickness, $180\text{-}\mu\text{m}$ thick for the yield optimized and $175\text{-}\mu\text{m}$ thick for the fall-line optimized designs, with 16% ($1038 \mu\text{g}$) and 15% ($933 \mu\text{g}$) mass remaining, respectively. The yield optimized design has an initial D-T fuel radius $R_0 = 265\text{-}\mu\text{m}$ with 0.24 g/cm^3 fill density, for a total fuel mass of $18.7 \mu\text{g}$ D-T. The fall-line optimized design has an initial fuel radius $R_0 = 215\text{-}\mu\text{m}$ with 0.2 g/cm^3 fill density, for a total fuel mass of $8.32 \mu\text{g}$.

The ablative-driven shock breaks out of the outer shell at around 3-ns for both designs, and the main shock propagates into the foam. The outward going rarefaction wave from the first shock release into the foam encounters the ablation front, and a steeping compression wave is reflected inward, driving a second shock into the foam at around 5-ns, which coalesces with the first shock before colliding with the inner shell. The outer shell obtains its maximum kinetic energy at about 6 ns as the drive diminishes. The shock collides with the outer surface of the inner shell about 6.28 ns for the fall-line design, and slightly earlier at 6.25 ns for the yield-optimized design, due to the slightly larger inner shell. The shock breaks out of the inner shell into the fuel at 6.685 and 6.7 ns for the max-yield and fall-line designs. The acceleration phase of the inner shell ends at 7.55 and 7.475 ns for the max-yield and fall-line designs, resulting in 20 kJ and 15.8 kJ of inner shell kinetic energy in each, or average pusher speed of 225 km/s and 242 km/s.

At the start of the deceleration phase, the internal energy of the D-T fuel is $\sim 1 \text{ kJ}$ and $\sim 0.75 \text{ kJ}$ for the max-yield and fall-line designs, and initial fuel pressures of 2.5 Gbar and 10 Gbar for each. For the burn-off (no alpha deposition) calculations, the stagnated fuel internal energy is 6.2 kJ and 3.8 kJ, respectively, yielding burn-off ion temperatures of 2.9 keV and 3.95 keV for the max-yield and fall-line designs. The no-burn areal densities are 0.51 g/cm^2 and 0.58 g/cm^2 ,

respectively, for the max-yield and fall-line designs. Calculations with alpha-deposition turned on give a 1-D yield of 2.11 MJ and 1.29 MJ for the max-yield and fall-line designs, with bang times of 7.963 ns and 7.695 ns, respectively.

One conservative metric to estimate the role of potential pusher mix into the fuel is to calculate the fall-line time of the pusher-fuel interface, i.e., the time at which the intercept of an extrapolated tangent line of the pusher at maximum velocity reaches zero radius.^{10,32} The fall-line marks the most inward radius mixing between the fuel and the pusher could reach if the mixed region were to continue traveling inward at the maximum pusher speed. A calculated fall-line time that coincides with the bang-time means that 50% of the burn is susceptible to mix. For the yield-optimized design, the fall-line intercepts $r=0$ at 7.91 ns, about 50-ps earlier than the bang time of 7.963-ns. The burn width for this design is about 60-ps, meaning that nearly all of the burn is susceptible to mix ($\sim 96\%$). For the fall-line optimized design, the fall-line intercept is at 7.685 ns, about 10-ps earlier than the bang time of 7.695 ns, with a burn width of 50-ps, meaning that about 65%–70% of the burn is susceptible to mix. These designs will be compared to the robust burn model described in Sec. VI, and we will examine the burn robustness in the presence of 2-D low-mode asymmetries from integrated calculations.

IX. 2-D LOW-MODE ASYMMETRY

Integrated 2-D HYDRA calculations of both the yield-optimized design and the fall-line optimized design are shown in Figs. 15(a) and 15(b) and 15(c) and 15(d). Both simulations used the same laser pulse shape and pointing to maintain identical radiation flux symmetry, and used integrated Monte Carlo radiation transport. The 1-D yield-optimized design was very marginal in 2-D, and only gave $\sim 2\%$ of the 1-D yield, 36 kJ in 2-D compared to 2.11 MJ in 1-D. In contrast, the 1-D fall-line optimized design was fairly robust in 2-D, and gave nearly 70% of the 1-D yield, 0.87 MJ in 2-D compared to 1.29 MJ in 1-D.

Figures 15(c) and 15(f) show the ion temperatures from the 1-D design calculations for the yield-optimized and fall-line optimized designs with α -deposition on (solid) and α -deposition off (dashed) near stagnation and bang time. With burn turned off, the stagnation temperature for the yield-optimized design is 2.9 keV, compared to only 5 keV with burn on at that time. While the temperature continues to increase in 1-D with burn on, the 2-D low-mode asymmetries are sufficient that the burn does not occur quickly enough before the hot spot disassembles, and the burn is quenched by PdV expansion cooling losses of the hot spot during the alpha-heating phase. Evaluation of the robust burn metric from Eq. (22) would require a no-burn stagnation

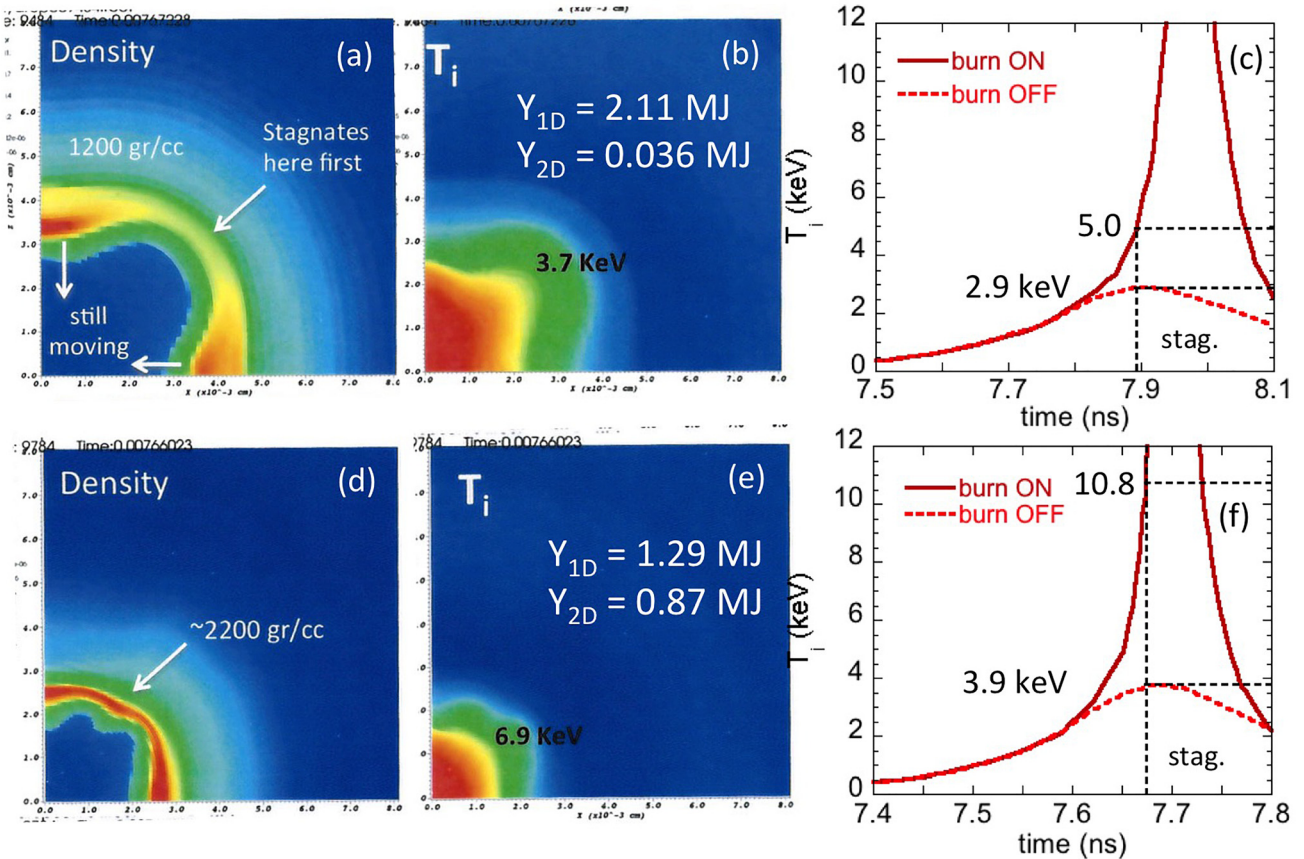


FIG. 15. Contour plots from 2-D integrated HYDRA simulations of the yield-optimized design showing (a) density and (b) ion temperature. Contour plots of (d) density and (e) ion temperature are shown in the lower panels for the fall-line optimized design. Plots of ion temperature with burn on (solid) and burn off (dashed) are shown for the (c) yield-optimized design and (f) fall-line optimized design. The fall-line design is more robust against low-mode asymmetries and burns quickly and more completely compared to the yield-optimized design due to the higher burn-off stagnation temperature (higher D-T specific internal energy).

temperature of 3.3 keV, above the 2.9 keV no-burn stagnation temperature. For this case, Eq. (22) was evaluated with the no-burn parameters for the yield-optimized design at stagnation of $T = 2.9$ keV, $\rho R_* = 0.51$ g/cm², $f_{\text{tamp}} = 3.5$, and a calculated $\hat{Q} = 0.9$. Note that the 2.9 keV stagnation temperature is larger than the 2.5 keV ignition temperature used in Ref. 23, which is obtained by only considering static losses due to radiation and conduction losses to the high-Z wall, and not the dynamic hot spot expansion losses which occur during the alpha-heating phase.

In comparison, Fig. 15(f) shows the ion temperatures, burn on and burn off, for the fall-line optimized design. With a smaller fuel mass, the 1-D no-burn ion temperature is 3.9 keV at stagnation, and is ~ 11 keV at stagnation with burn on. In this case, the larger stagnation temperature means that the burn is more vigorous, $\langle \sigma v \rangle \sim T^4$ in this temperature regime, and the 2-D yield is only slightly degraded from the 1-D yield in the presence of low-mode asymmetries. The burn metric from Eq. (22) indicates that α -heating will exceed hot spot expansion losses when the stagnation temperature is greater than $T > 3.1$ keV, evaluated for no-burn $T = 3.9$ keV, $\rho R_* = 0.58$ g/cm², $f_{\text{tamp}} = 3.5$, and a calculated $\hat{Q} = 0.9$.

Note that for both the yield-optimized and fall-line optimized designs in Figs. 15(c) and 15(f) the burn-on ion temperature begins to deviate from the burn-off temperature at ~ 2.5 keV. If the confinement time during burn was sufficiently large, then this static ignition temperature of ~ 2.5 keV would be a sufficient metric for a large fraction of burn to occur. However, since the rate of α -heating is competing with the rate of hot spot disassembly (and cooling), one requires a higher temperature at stagnation to ensure a large fraction of fuel burn before hot spot disassembly. This is similar to recent results discussed by Springer³³ for single-shell capsule designs, where they differentiate between a hot spot temperature increase $\partial T / \partial t > 0$ to overcome static radiation and conduction losses, but require $\partial^2 T / \partial t^2 > 0$ to overcome dynamic expansion cooling losses of the hot spot. As a final note, requiring a stagnation temperature larger than the robust burn metric of Eq. (22) for our designs means that the static ignition temperature of ~ 2.5 keV is reached substantially before stagnation, i.e., “upstream ignition.”²³ Thus, since ignition starts before the hot spot is fully compressed at stagnation in the fall-line optimized design, it is less sensitive to low-mode asymmetries. In contrast, the yield-optimized design marginally meets the robust burn criterion of Eq. (22) in 1-D so that the same 2-D low mode asymmetries lead to lower stagnation temperatures in 2-D than in 1-D, and only an insignificant amount of burn occurs before disassembly cools the hot spot.

X. PERTURBATIVE SCALING WITH ABSORBED ENERGY

While more exhaustive design studies should be performed, it is instructive to examine the improvement in performance (fuel specific internal energy) for more absorbed energy in the outer shell. Rather than completely changing the design, we simply consider keeping the fuel radius, fuel mass, inner shell and tamper thickness fixed, and the outer

shell thickness fixed, while increasing the outer shell radius perturbatively from scale $S_{\text{out}} = 1.0$ –1.2. The calculations were performed in 1-D HELIOS using the radiation temperature and fall-line optimized design from the 1-D HYDRA calculations as the $S_{\text{out}} = 1.0$ case, and were performed with burn turned off. As stated before, the 1-D HELIOS calculations are in fairly good agreement with bang-time, kinetic energies of the ablator and pusher, hot spot convergence, and internal energy using a Au-pusher, compared to a W-pusher for the 1-D HYDRA calculations. The Al outer shell thickness was fixed at 175- μm as the outer shell radius was scaled from 1.11-mm ($S_{\text{out}} = 1$) to 1.332-mm ($S_{\text{out}} = 1.2$). The kinetic energy of the outer shell, kinetic energy of the inner shell, and the fuel internal energy (fixed mass) are shown normalized to the $S_{\text{out}} = 1$ values in Fig. 16 versus the outer shell scale factor S_{out} . The outer shell kinetic energy increases as $\sim S_{\text{out}}^{2.5}$ as might be roughly expected since, for fixed radiation temperature, the absorbed energy scales as the outer shell surface area, $\sim S_{\text{out}}^2$, and there is a correction for payload mass (unablated mass) described in Saillard.¹⁸ Since the outer shell mass with fixed thickness scales roughly as $\sim S_{\text{out}}^2$ and the outer shell kinetic energy scales as $\sim S_{\text{out}}^{2.5}$, the outer shell velocity increases weakly as $\sim S_{\text{out}}^{0.25}$. Both the inner shell kinetic energy and the fuel specific internal energy scale as $\sim S_{\text{out}}^{1.5}$ up to a scale of ~ 1.05 , but the inner shell kinetic energy rolls over, while the fuel internal energy continues to increase as $\sim S_{\text{out}}^{1.5}$ up to a scale factor of 1.15, and then also diminishes for larger S_{out} . Due to the larger outer shell, more compression occurs in the foam cushion, leading to larger initial drive pressures on the inner shell, but since the shock and rarefaction transit times

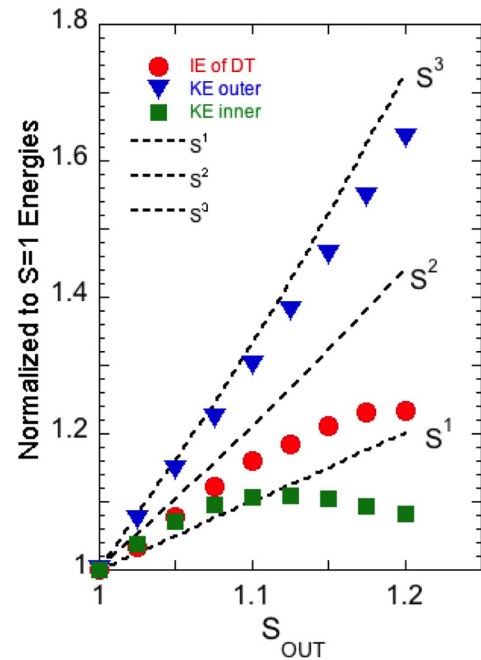


FIG. 16. Normalized energies versus outer shell scale factor S_{OUT} for outer shell kinetic energy (triangles), inner shell kinetic energy (squares), and D-T internal energy (circles) from 1-D HELIOS simulations, burn off. The dashed lines are simply guides showing scaling as S^1 , S^2 , or S^3 . Note that D-T internal energy continues to increase with outer shell scale factor S_{OUT} , despite inner shell kinetic energy rolling over for $S_{\text{OUT}} > 1.1$.

decrease compared to the $S_{out} = 1$ case, an overall lower drive pressure and lower inner shell kinetic energy are the result. However, the initial pressure of the fuel increases during the acceleration phase as the initial shock pressure increases due to larger spherical convergence effects, so the fuel internal energy continues to increase despite a decreasing inner shell kinetic energy. As the outer shell scale increases beyond 1.15, little margin is gained in fuel internal energy since the inner shell kinetic energy is decreasing more rapidly.

This simple perturbative scaling shows that the fuel specific internal energy scales slightly faster than outer shell scale size, $SIE \sim S_{out}^{1.5}$, not quite as fast as gains in outer shell kinetic energy, $KE_{out} \sim S_{out}^{2.5}$. Based on our results in Sec. IV, the main shock will be stronger from spherical convergence effects due to a smaller size inner shell with respect to outer shell, and less kinetic energy will be coupled from outer to inner as the ratio between outer and inner shell radii increases. These trends in performance are qualitatively understood for small outer shell scale changes. Other increases in performance margin may be gained by optimizing the inner shell radius and shell thicknesses for increased outer shell energy, but is beyond the scope of this current paper.

XI. SUMMARY AND CONCLUSIONS

Double shell capsules offer a potential low hot spot convergence ratio path to robust burn and possible ignition, and trade some of the physics challenges found in single shell capsules for complexity in building and diagnosing double shells. Despite the complexity of extra interfaces and the vast array of design choices that double shells require compared to single shell capsule implosions, some simple physically based models are developed to describe the various stages of a double shell implosion and its performance, as well as guiding the selection of the various design choices. A robust burn metric is developed that sets a minimum no-burn stagnation temperature required for α -heating to exceed the dynamic hot spot expansion losses during burn. This robust burn metric delineates poorly burning capsules from robustly burning capsules in the presence of similar low-mode asymmetries. Future simulation and experimental research will examine burn performance in the presence of high-mode instabilities, and jets due to engineering artifacts, such as the fill-tube and outer shell joint. Present design efforts have been intentionally constrained by current manufacturing capabilities, but can be expanded as advanced manufacturing capabilities become mature, such as the use of graded density pushers.^{11,30}

ACKNOWLEDGMENTS

We acknowledge the useful discussions with Jas Mercer-Smith, Nelson Hoffmann, John Kline, Austin Yi, and Cris Barnes at LANL, Haibo Huang at General Atomics, and Frank Graziani, Jesse Pino, and Daniel Clark at LLNL. Steven Batha was the LANL ICF Program Manager who funded this research. This work was performed under the auspices of the U.S. Department of Energy by Los Alamos National Laboratory under Contract No. DE-AC52-06NA25396.

APPENDIX A: PRESSURE IONIZATION OF A HIGH-Z PUSHER

This work was first reported by Rosen^{34,35} and is generalized here. For a high-Z inner shell compressed to 1500–2500 g/cm³, it is ionized due to pressure ionization, and its electrons remain very nearly Fermi-degenerate, despite the Gbar-scale shocks traversing through the material during acceleration and deceleration phases. It is useful to derive estimates using a Thomas-Fermi like model for the high-Z shell parameters near stagnation. Recall that the Fermi energy for electrons in cold compressed matter is

$$\varepsilon_{FD} = \frac{h^2}{2m_e} \left(\frac{3}{8\pi} n_e \right)^{2/3}, \quad (\text{A1})$$

where m_e and n_e are the electron mass and number density and h is Planck's constant. Assuming a mass density ρ , and ionization state Z for matter of atomic mass number A , and using $n_e = ZN_A\rho/A$, where N_A is Avogadro's number, we find

$$\varepsilon_{FD} \approx 26 \left(\frac{Z}{A} \right)^{2/3} \rho^{2/3} \text{ eV}, \quad (\text{A2})$$

where the mass density ρ is given in g/cm³. Gold metal at room temperature has roughly $Z \approx 1$ in the conduction band, and has a Fermi energy of $\varepsilon_{FD} \approx 5.5$ eV. In cold Fermi-degenerate matter, the pressure is mostly from the electrons, $P_{FD} = (2/5)n_e\varepsilon_{FD}$, or in practical units

$$P_{FD} \approx 10\rho^{5/3} \left(\frac{Z}{A} \right)^{5/3} [\text{Mbar}]. \quad (\text{A3})$$

We need to find the ionization state Z due to pressure ionization of the compressed high-Z material. We use a highly simplified Thomas-Fermi like approach (with non-interacting electrons) where the principal quantum number n_p is averaged over the atom to obtain the number of bound electrons Z_{bnd} , where the average ionization state we are trying to determine is $Z = Z_N - Z_{bnd}$, and Z_N is the atomic number of the neutral atom. Then

$$Z_{bnd} = \int_0^{n_p} 2n^2 dn = (2/3)n_p^3. \quad (\text{A4})$$

Employing the Bohr hydrogenic atom ionization potential, and the bound electrons in Eq. (A4)

$$I_Z = Z^2 E_H / n_p^2 = Z^2 E_H ((2/3)/Z_{bnd})^{2/3}, \quad (\text{A5})$$

where $E_H = 13.6$ eV is the hydrogen ionization potential. Defining the fraction of electrons ionized as $X \equiv Z/Z_N$, the ionization energy is then

$$I_Z = Z_N^{4/3} E_H (2/3)^{2/3} X^2 / (1 - X)^{2/3}. \quad (\text{A6})$$

The ionization fraction part can be approximated by a power-law fit in the vicinity of 60% ionization ($X = 0.6$), i.e., $X^2/(1 - X)^{2/3} \approx 0.66(X/0.6)^{3.1}$, so that

$$I_Z \approx Z_N^{4/3} E_H (2/3)^{2/3} (0.66(X/0.6)^{3.1}). \quad (\text{A7})$$

To self-consistently find Z , we equate this ionization potential I_Z to the Fermi energy Eq. (A2), and find the ionization state as a function of density

$$Z \approx 0.212 \cdot Z_N \left(\frac{1}{Z_N} \right)^{0.274} \left(\frac{197}{A} \right)^{0.274} \rho^{0.274}. \quad (\text{A8})$$

For Au ($Z_N = 79$, $A = 197$), the ionization state $Z_{Au} \approx 5.05 \rho^{0.274}$, and for W ($Z_N = 74$, $A = 184$), the ionization state is $Z_W \approx 4.91 \rho^{0.274}$. Using the generalized form Eq. (A8), assuming ionization fraction around 60% or so, and inserting into Eq. (A3), we have

$$P_{FD} \approx 8.32 Z_N^{1.21} \left(\frac{\rho}{A} \right)^{2.123} [\text{Mbar}]. \quad (\text{A9})$$

Using these estimates, Au would need to be compressed to $\rho_{Au} \sim 2600 \text{ g/cm}^3$ to achieve 400 Gbar pressures ($Z_{Au} \approx 43.5$), a slightly lower predicted compression compared to $\rho_{Au} \sim 2800 \text{ g/cm}^3$ from the SESAME table for 400 Gbar. It is tempting to use Eq. (A9) at stagnation for Eq. (17) in Sec. V for the high-Z pusher and derive a similar Fermi-degenerate expression for internal energy. However, one would need to also include the electron-ion and electron-electron Coulomb interactions to obtain a sufficiently accurate model for the internal energy in this regime,³⁶ but such an inclusion is beyond the scope of this present paper. Further, it is only the unshocked region of the thick pusher²² that remains nearly Fermi-degenerate. The shocked region in contact with the D-T fuel during deceleration phase is relatively incompressible in comparison. This highlights the difficulty and limitations of a simple quasi-adiabatic compression model during stagnation to infer the partition of kinetic energy into internal energies, as in Sec. V, when treating the entire pusher as compressible. Thus, Eqs. (A8) and (A9) should only be used to obtain simple estimates of compressed pusher parameters.

APPENDIX B: PUSHER AND GAS INITIAL CONDITIONS DURING ACCELERATION

1. Fit to Au Hugoniot

For useful estimates of a Au shell during its acceleration phase, we show below fits to the Au SESAME equation of state (EOS) table in the range 0.2–10 Gbar. Assuming the initial shock and pressure drive P_D puts the Au shell at initial density $\rho_0 = 19.3 \text{ g/cm}^3$ on Hugoniot, the pressure in the Au is $P_D = \rho_0 u_s u_p$, which in the strong shock limit is $P_D = [(\gamma_s + 1)/2] \rho_0 u_p^2$. The density compression is $(\gamma_s + 1)/(\gamma_s - 1)$. To good approximation, the specific internal energy of the shocked Au is $\varepsilon \approx u_p^2/2$.

The fit of the adiabatic index γ_s on the Hugoniot for Au is parameterized quadratically with the logarithm of P_D between 0.2–10 Gbar

$$\gamma_s \approx \gamma_0 + \gamma_1 \cdot \log(P_D) + \gamma_2 \cdot \log(P_D)^2, \quad (\text{B1})$$

where P_D is in Gbar, $\gamma_0 = 1.513$, $\gamma_1 = -0.1811$, and $\gamma_2 = 0.1045$. The fit yields $\gamma_s = 1.5$ at $P_D = 1.186 \text{ Gbar}$.

Given the pressure P_D and the adiabatic index γ_s , the density compression, particle speed u_p , and specific internal energy can be found.

2. Derivation of gas pressure upon initial shell release

Consider a dense shell with density ρ_s and adiabatic index γ_s , driven at constant pressure P_D , which releases into a lower density gas with density ρ_0 and adiabatic index γ . Using the shock jump conditions and the strong shock relations, the pressure in the dense shell is related to the particle speed as

$$P_D = \rho_s u_s u_p \approx \left(\frac{\gamma_s + 1}{2} \right) \rho_s u_p^2. \quad (\text{B2})$$

Upon release of the shock into the gas, the particle speed in the gas roughly doubles from that in the shell, $u \approx 2u_p$, and the initial pressure in the gas P_i is

$$P_i \approx \left(\frac{\gamma + 1}{2} \right) \rho_0 (2u_p)^2,$$

which after substituting the particle speed from Eq. (B2), we have

$$P_i \approx 4P_D \left(\frac{\gamma + 1}{\gamma_s + 1} \right) \left(\frac{\rho_0}{\rho_s} \right), \quad (\text{B3})$$

which then yields the ρ_0/ρ_s scaling for the initial gas pressure used in Eq. (14).

Equation (B3) is in good agreement with hydrodynamic simulations for the initial gas pressure after shock release from the shell, but as discussed in the text, convergence affects, shock, and rarefaction reverberation in the finite thickness shell, and the fact that the entire gas volume has not yet been shock heated during acceleration means that only the scaling with drive pressure and gas/shell density ratios are reliable for use in Eq. (14) for this thin shell treatment.

¹E. M. Campbell and W. J. Hogan, *Plasma Phys. Controlled Fusion* **41**, B39 (1999).

²E. I. Moses, *J. Phys. Conf. Ser.* **112**, 012003 (2008).

³J. Lindl, *Phys. Plasmas* **2**, 3933 (1995).

⁴J. D. Lindl, P. Amendt, R. L. Berger, S. G. Glendinning, S. H. Glenzer, S. W. Haan, R. L. Kauffman, O. L. Landen, and L. J. Suter, *Phys. Plasmas* **11**, 339 (2004).

⁵D. S. Clark, S. W. Haan, B. A. Hammel, J. D. Salmonson, D. A. Callahan, and R. P. J. Town, *Phys. Plasmas* **17**, 052703 (2010).

⁶S. W. Haan, J. D. Lindl, D. A. Callahan, D. S. Clark, J. D. Salmonson, B. A. Hammel, L. J. Atherton, R. C. Cook, M. J. Edwards, S. Glenzer, A. V. Hamza, S. P. Hatchett, M. C. Herrmann, D. E. Hinkel, D. D. Ho, H. Huang, O. S. Jones, J. Kline, G. Kyrala, O. L. Landen, B. J. MacGowan, M. M. Marinak, D. D. Meyerhofer, J. L. Milovich, K. A. Moreno, E. I. Moses, D. H. Munro, A. Nikroo, R. E. Olson, K. Peterson, S. M. Pollaine, J. E. Ralph, H. F. Robey, B. K. Spears, P. T. Springer, L. J. Suter, C. A. Thomas, R. P. Town, R. Vesey, S. V. Weber, H. L. Wilkens, and D. C. Wilson, *Phys. Plasmas* **18**, 051001 (2011).

⁷D. S. Clark, C. R. Weber, J. L. Milovich, J. D. Salmonson, A. L. Kritcher, S. W. Haan, B. A. Hammel, D. E. Hinkel, O. A. Hurricane, O. S. Jones, M. M. Marinak, P. K. Patel, H. F. Robey, S. M. Sepke, and M. J. Edwards, *Phys. Plasmas* **23**, 056302 (2016).

⁸O. A. Hurricane, D. A. Callahan, D. T. Casey, P. M. Celliers, C. Cerjan, E. L. Dewald, T. R. Dittrich, T. Döppner, D. E. Hinkel, L. F. Berzak Hopkins, J. L. Kline, S. Le Pape, T. Ma, A. G. MacPhee, J. L. Milovich,

- A. Pak, H. S. Park, P. K. Patel, B. A. Remington, J. D. Salmonson, P. T. Springer, and R. Tommasini, *Nature* **506**, 343 (2014).
- ⁹W. S. Varnum, N. D. Delameter, S. C. Evans, P. L. Gobby, J. E. Moore, J. M. Wallace, R. G. Watt, J. D. Colvin, R. Turner, V. Glebov, J. Soures, and C. Stoeckl, *Phys. Rev. Lett.* **84**, 5153 (2000).
- ¹⁰P. Amendt, J. D. Colvin, R. E. Tipton, D. E. Hinkel, M. J. Edwards, O. L. Landen, J. D. Ramshaw, L. J. Suter, W. S. Varnum, and R. G. Watt, *Phys. Plasmas* **9**, 2221 (2002).
- ¹¹J. L. Milovich, P. Amendt, M. Marinak, and H. Robey, *Phys. Plasmas* **11**, 1552 (2004).
- ¹²S. A. Colgate and A. G. Petschek, "Minimum conditions for the ignition of fusion: A realistic interim goal for inertial fusion," Los Alamos National Laboratory Internal Report No. LA-UR-88-1268 (1988); copies may be obtained from the National Technical Information Service, Springfield, VA.
- ¹³A. Yi, LANL, private communication (2017).
- ¹⁴D. Clark, LLNL, private communication (2017).
- ¹⁵B. A. Hammel, S. W. Haan, D. S. Clark, M. J. Edwards, S. H. Langer, M. M. Marinak, M. V. Patel, J. D. Salmonson, and H. A. Scott, *High Energy Density Phys.* **6**, 171 (2010).
- ¹⁶H. F. Robey, P. M. Celliers, J. D. Moody, J. Sater, T. Parham, B. Kozioziemski, R. Dylla-Spears, J. S. Ross, S. LePape, J. E. Ralph, M. Hohenberger, E. L. Dewald, L. Berzak Hopkins, J. J. Kroll, B. E. Yoxall, A. V. Hamza, T. R. Boehly, A. Nikroo, O. L. Landen, and M. J. Edwards, *Phys. Plasmas* **21**, 022703 (2014).
- ¹⁷R. E. Olson and R. J. Leeper, *Phys. Plasmas* **20**, 092705 (2013).
- ¹⁸Y. Saillard, *Nucl. Fusion* **46**, 1017 (2006).
- ¹⁹M. M. Marinak, G. D. Kerbel, N. A. Gentile, O. Jones, D. Munro, S. Pollaine, T. R. Dittrich, and S. W. Haan, *Phys. Plasmas* **8**, 2275 (2001).
- ²⁰J. von Neumann, *Collected Works* (MacMillan, New York, 1963), Vol. VI.
- ²¹J. J. MacFarlane, I. E. Golovkin, and P. R. Woodruff, *J. Quant. Spectrosc. Radiat. Trans.* **99**, 381 (2006).
- ²²R. Betti, K. Anderson, V. N. Goncharov, R. L. McCrory, D. D. Meyerhofer, S. Skupsky, and R. P. J. Town, *Phys. Plasmas* **9**, 2277 (2002).
- ²³K. Molvig, M. J. Schmitt, B. J. Albright, E. S. Dodd, N. M. Hoffman, G. H. McCall, and S. D. Ramsey, *Phys. Rev. Lett.* **116**, 255003 (2016).
- ²⁴O. N. Krokhin and V. B. Rozanov, *Sov. J. Quantum Electron.* **2**, 393 (1973).
- ²⁵R. C. Kirkpatrick and J. A. Wheeler, *Nucl. Fusion* **21**, 389 (1981).
- ²⁶R. S. Cooper and F. Evans, *Phys. Fluids* **18**, 332 (1975).
- ²⁷Y. B. Zel'dovich and Y. P. Raizer, *Physics of Shock Waves and High-Temperature Hydrodynamic Phenomena* (Academic, New York, 1966).
- ²⁸R. W. Margevicius, L. J. Salzer, M. A. Salazar, and L. R. Foreman, *J. Fusion Technol.* **35**, 106 (1999).
- ²⁹E. C. Merritt, E. N. Loomis, D. C. Wilson, T. Cardenas, D. S. Montgomery, W. S. Daughton, E. S. Dodd, T. Desjardins, D. B. Renner, S. Palaniyappan *et al.*, *Bull. Am. Phys. Soc.* **62**(7.3), 221 (2017).
- ³⁰H. Huang, General Atomics, private communication (2017).
- ³¹E. Loomis, W. Daughton, D. S. Montgomery, D. C. Wilson, E. Merritt, J. P. Sauppe, E. S. Dodd, S. Palaniyappan, R. Sacks, T. Cardenas *et al.*, "Assessing sources of low-mode asymmetries and shape transfer in double shell targets with integrated radiation hydrodynamic simulations," *Phys. Plasmas* (unpublished).
- ³²L. Welser-Sherrill, J. H. Cooley, D. A. Haynes, D. C. Wilson, M. E. Sherrill, R. C. Mancini, and R. Tommasini, *Phys. Plasmas* **15**, 072702 (2008).
- ³³P. T. Springer, O. A. Hurricane, J. H. Hammer, R. Betti, D. A. Callahan, E. M. Campbell, D. T. Casey, C. J. Cerjan, D. Cao, M. J. Edwards *et al.*, "A 3D dynamic model to assess impacts of low-mode asymmetry, aneurysms, and mix induced radiative loss on capsule performance at NIF, Omega, and Z," in *Inertial Fusion Sciences and Applications* (IOP Science, St. Malo, France, 2017).
- ³⁴M. D. Rosen, "A simple model for ICF double shell target performance," Lawrence Livermore National Laboratory Internal Report No. UCRL-PRES-235758 (2007).
- ³⁵M. D. Rosen, *Bull. Am. Phys. Soc.* **52**, 149 (2007).
- ³⁶R. M. More, K. H. Warren, D. A. Young, and G. B. Zimmerman, *Phys. Fluids* **31**, 3059 (1988).
- ³⁷G. S. Fraley, E. J. Linnebur, R. J. Mason, and R. L. Morse, *Phys. Fluids* **17**, 474 (1974).
- ³⁸J. H. Hammer and M. D. Rosen, *Phys. Plasmas* **10**, 1829 (2003).